Cell-Free IoT Networks with SWIPT: Performance Analysis and Power Control Policy

Yao Zhang, Wenchao Xia, *Member, IEEE*, Haitao Zhao, *Member, IEEE*, Wei Xu, *Senior Member, IEEE*, and Longxiang Yang

***Abstract*—In this paper, the performance of simultaneous wireless information and power transfer (SWIPT) in downlink (DL) Internet-of-things (IoT) networks relying on cell-free massive multiple-input multiple-output (CF-mMIMO) technology is investigated. In such a network, the access points (APs) beam radio-frequency (RF) energy toward the IoT sensors during the DL phase of wireless power transfer. Tight closed-form expressions for the DL harvested energy (HE) and achievable rate with conjugate beamforming (CB) and normalized CB (NCB) are respectively derived, which enable us to analyze the HE-rate trade-offs under different precoding techniques. Apart from this, to guarantee the sensor fairness with respect to the HE and achievable rate, a max-min fairness power control algorithm based on the accelerated projected gradient (APG) method is proposed. Specifically, the proposed APG-based algorithm is able to determine the optimum of the considered max-min fairness problem in closed form and is more memory-efficient than traditional convex-solver-based counterparts. These analytical results as well as the effectiveness of the proposed power control policy are verified by experimental simulations.**

***Index Terms*—Simultaneous wireless information and power transfer (SWIPT), Internet-of-things (IoT), cell-free massive multiple-input multiple-output (CF-mMIMO), max-min power control, accelerated projected gradient (APG).**

I. Introduction

RECENTLY, the Internet-of-thing (IoT) architecture has been regarded as a promising wireless standard for the beyond fifth-generation (B5G) and sixth-generation (6G) communication networks [1]–[4], for its ability to enable smart city and intelligent manufacturing by connecting a great number of smart sensors with each other to realize the information-sharing and decision-making coordination. However, the underlying benefits of IoT networks are severely bottlenecked by the limited battery capacities of IoT sensors [5].

To prolong the lifetimes of the sensors and alleviate the issue of energy shortage in IoT networks, an attractive solution is the simultaneous wireless information and power transfer (SWIPT) [6]–[8], which can be treated as a supplementary wireless energy source to sensors. In the context of the SWIPT-based time-switching (TS) receiver protocol, in which the radio-frequency (RF) energy transfer and information reception occur orthogonally in time domain, the sensors first capture the wireless RF energy emitted by the distributed access points (APs) during a small portion of the downlink (DL) data transmission phase and then receive the payload information symbols throughout the remaining DL time-slots [9]. In fact, the dominant inhibiting factor for enabling SWIPT in practice is the inherent long distance between the transmitter and receiver, which can result in significant end-to-end pathloss and severely hamper the energy harvesting and information decoding efficiencies [8]–[10]. To this end, the cellular massive multiple-input multiple-output (mMIMO) technology, which admits robust channel hardening and aggressive spatial multiplexing gains by deploying a large number of antenna arrays at base stations (BSs), has been recommended by researchers to tackle the above issues since it can steer more RF energy and information beams toward the intended sensors [11]–[16]. The DL achievable rate of an mMIMO SWIPT system over Rician fading channels was analyzed in [14] and the impacts of channel reciprocity error were studied in [15]. In addition, Goli *et al.* [16] investigated the DL of a multiuser mMIMO SWIPT system in terms of secrecy rate maximization. Those contributions indicated that the mMIMO architecture is able to broaden the application prospect of SWIPT and accelerate the deployment of SWIPT in practice. Although the large-scale antenna architecture helps enhance the energy capturing and information reception efficiencies for a vast majority of sensors, the system performance of cell-edge sensors is still hindered by heavy pathloss [17]–[20].

Nowadays, the cell-free mMIMO (CF-mMIMO) technique [21] has been proved to be able to significantly boost the spectral and energy efficiencies [22]–[24]. In a CF-mMIMO system, a few antennas are gathered into an AP and plenty of APs are spread out over a large area and coherently communicate with a small number of sensors in the same time-frequency resource units. This distributed system can be implemented by using simple precoding/detection processing which facilitates the exploitation of phenomena such as favorable propagation and channel hardening. Besides, all the APs are connected to a central server (CS) through the robust fronthaul networks to exchange useful information and signaling. Indeed, compared with a traditional cellular mMIMO, the cell-boundaries vanish in the CF case and the ubiquitous distribution of APs contribute to alleviating substantial performance degradations of cell-edge sensors by shortening the communication distances between the terminals and served APs [17], [18].

In view of the fascinating merits of cellular mMIMO SWIPT

Yao Zhang is with the College of Physics and Electronic Information Engineering, Zhejiang Normal University, Jinhua 321004, China. Email: zhangyao94@126.com.

Wei Xu is with the National Mobile Communications Research Lab., Southeast University, Nanjing 210096, China. Email: wxu@seu.edu.cn

Wenchao Xia, Haitao Zhao, and Longxiang Yang are with the Department of Wireless Communication Key Lab of Jiangsu Province, Nanjing University of Posts and Telecommunications, Nanjing 210003, China. Email: {xiawenchao, zhaoht, yanglx}@njupt.edu.cn.

systems, the combination of CF-mMIMO-based IoT network with SWIPT furnishes a great potential to further improve the harvested energy (HE) and achievable rate. However, a common concern in CF-mMIMO-based IoT SWIPT networks is that the wide distribution of the IoT sensors may lead to severe performance differentiation. To address this issue, the max-min fairness power control policy, which is realized by dynamically adjusting the transmit power of APs and renders uniformly good service for all sensors, has been extensively studied in recent years [25]. Due to the DL energy transfer and information reception occur in two orthogonal time-slots in the context of TS receiver protocol, the AP transmit power can be separately optimized in the corresponding phases to maximize the minimum HE and achievable rate. In this regard, many studies have resorted to off-the-shelf convex solvers to determine the numerical optimums of the considered max-min fairness problems [21], [26]–[28]. For concise, we denote this approach as the convex-solver-based max-min fairness power control. Specifically, a max-min fairness HE power control policy was studied in [26], where the bisection method was used to numerically find the optimal power control coefficients. Besides, Ngo *et al.* [21] focused on the sensor rate fairness and proposed max-min rate power control algorithms for both uplink (UL) and DL CF-mMIMO networks. To further boost the maximized uniform rate, a receiver filter design together with the max-min power control was presented in [27] and [28]. Nevertheless, these power control strategies were basically executed by using the interior-point algorithm, which not only makes the computational complexity unable to scale favorably with the network size but also limits previous analyses of power control in CF-mMIMO networks to small and medium scales.

In light of the above, a DL CF-mMIMO-based IoT SWIPT network is studied in this paper. We adopt two different precoding techniques in DL, namely conjugate beamforming (CB) and normalized CB (NCB). In [29], Interdonato *et al.* pointed out that the NCB scheme helps improve the achievable rate by reducing the beamforming gain uncertainty as compared to the CB one, but whether the NCB scheme outperforms the CB scheme in terms of HE is still unclear. Besides, we also design an accelerated projected gradient (APG)-based max-min fairness power control policy with fast executing speed [30]–[32] to obtain the maximized identical HE and achievable rate. The contributions of this paper are outlined as follows.

1) We develop a framework for analyzing both the DL HE and achievable rate in a CF-mMIMO-based IoT SWIPT network with CB and NCB schemes. Exact closed-form expressions for the underlying performance metrics are respectively derived. In particular, the tractability of the obtained closed-form results facilitates exploring the HE-rate trade-offs under both the CB and NCB schemes.
2) To tackle the scalability of power control in the CF-mMIMO-based IoT SWIPT network, the APG optimization method is utilized to accelerate the executing speed of the max-min fairness power control algorithm. We stress that the proposed APG-based max-min policy can achieve the optimum of the optimization problem in closed form and admit a higher storage efficiency, thus possessing a faster computing speed. Most importantly, it also ensures sensor fairness in terms of HE and achievable rate regardless of the sensor locations.
3) Numerical simulations are given to verify our analytical derivations and corroborate the effectiveness of the proposed power control policy. Compared with the CB technique, it is observed that the NCB counterpart benefits from a better DL achievable rate but performs unsatisfactorily in capturing RF energy. Besides, the presented APG-based max-min fairness power control policy possesses a faster execution speed and a higher storage efficiency as compared to the traditional convex-solver-based one.

TABLE I
NOTATIONS

Notation	Meaning
$\mathbf{A}^H, \mathbf{A}^T, \mathbf{A}^*$	The conjugate transpose, transpose, and conjugate of matrix $\mathbf{A}$
$\text{diag}(\mathbf{A})$	The diagonal matrix consisting of the diagonal entries of matrix $\mathbf{A}$
$[\mathbf{A}]_n$	The nth column of matrix $\mathbf{A}$
∇f	The derivation of function f
$\|\| \cdot \|\|$	Euclidean norm operator
$\| \cdot \|$	Determinant or modulus operator depending on context
$\mathbb{E}\{\cdot\}$	Expectation operator
$\mathbb{C}$	Set of complex numbers
$\mathbf{I}_N,\ \mathbf{0}_N$	Identity matrix and zero matrix of size $N \times N$
$\mathbf{n} \sim \mathcal{N}_{\mathbb{C}}(\mathbf{0}_N, \mathbf{I}_N)$	Circularly symmetric complex Gaussian random vector with mean $\mathbf{0}_N$ and covariance $\mathbf{I}_N$

The remainder of this paper is outlined as follows. Section II briefly shows the CF-mMIMO-based IoT SWIPT model and gives the wirelessly powered time-division-duplex (TDD) transmission frame. In Section III, we derive closed-form HE and rate expressions with both CB and NCB techniques. Besides, Section IV presents the APG-based max-min HE power control algorithm and Section V details the APG-based max-min rate power control algorithm. Moreover, Section VI conducts experimental simulations and Section VII concludes this paper.

Notations: Small boldface letters denote column vector and capital boldface letters are matrices. Other notations that appeared in this paper are summarized in Table I, shown at the top of this page.

II. CF-mMIMO-based IoT SWIPT Network and Transmission Models

This work considers a wirelessly powered DL CF-mMIMO-based IoT network operating in TDD mode with L uniformly distributed N-antenna APs and K_{Total} single-antenna IoT sensors. All L APs are supposed to be linked to the CS through the lossless fronthaul networks. Besides, among K_{Total} sensors only K active sensors (ASs) denoted as AS_1, AS_2, ..., AS_K are communicated with all APs at any given moment, see Fig.

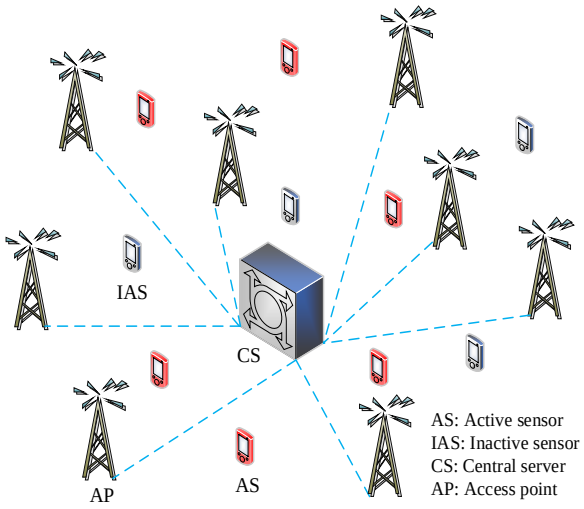

Fig. 1. A wirelessly powered CF-mMIMO-based IoT network with active and inactive sensors. Each sensor is equipped with both information and energy receivers.

1, shown at the top of the next page. All sensors are equipped with both information and energy receivers and harvest the RF energy emitted by the APs based on the TS receiver protocol. The captured power is typically stored or used to charge the batteries of ASs. In this work, we focus on the DL data transmission and assume that each coherence interval of τ_{c} symbols is split into three orthogonal phases with lengths of τ_{p}, $\alpha\tau_{\mathrm{d}}$, and $(1-\alpha)\,\tau_{\mathrm{d}}$, namely the UL training, DL energy transfer, and DL information reception phases, see Fig. 2. Here, τ_{p} and τ_{d} refer to the time lengths of UL training and DL transmission in each coherence interval. Besides, α denotes the TS factor which aims to strike a dynamic balance between energy harvesting and information reception.

In this work, we focus on the slow time-varying block Rayleigh fading scenario [21], [22] and the channel response from $\mathrm{AP}_l, \forall l$ to $\mathrm{AS}_k, \forall k$ is generated as $\mathbf{g}_{lk} = \sqrt{\beta_{lk}}\mathbf{h}_{lk} \in \mathbb{C}^{N\times 1}$, with β_{lk} and $\mathbf{h}_{lk} \sim \mathcal{N}_{\mathbb{C}}\left(\mathbf{0}_N, \mathbf{I}_N\right)$ being the large-scale fading coefficient and small-scale fading vector, respectively. Focusing on β_{lk}, it can be expressed as the product of the shadow fading z_{lk} and pathloss PL_{lk} (measured in dB) [21], where $z_{lk} \sim \mathcal{N}_{\mathbb{C}}\left(0, \sigma_{\mathrm{sh}}\right)$ with σ_{sh} being the standard deviation and

$$\mathrm{PL}_{lk} = \begin{cases} -140.7 - 35\log_{10}(d_{lk}), & \text{if } d_{lk} > d_1, \\ -140.7 - 15\log_{10}(d_1) - 20\log_{10}(d_{lk}), & \\ \qquad\qquad \text{if } d_0 < d_{lk} \leqslant d_1, & (1) \\ -140.7 - 15\log_{10}(d_1) - 20\log_{10}(d_0), & \\ \qquad\qquad \text{if } d_{lk} \leqslant d_0. & \end{cases}$$

Note that in (1), d_{lk} (in km) is the distance between AP_l and AS_k. In the following, the UL channel state information (CSI) acquisition is detailed first.

A. UL Training

Conventionally, in pilot-based channel estimation, all K ASs are required to simultaneously emit the pre-assigned pilot sequences of τ_{p} symbols to the APs for channel estimation.

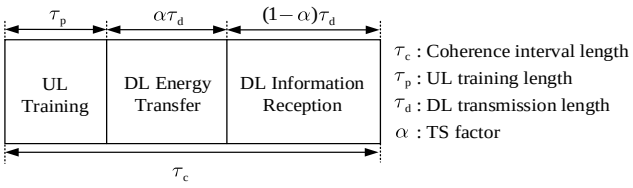

Fig. 2. A wireless powered TDD transmission frame.

Note that when the AS number exceeds the pilot length, pilot reuse is necessary for different sensors, which gives rise to the pilot contamination. In this work, we consider a heavily-loaded IoT network with $K \geqslant \tau_{\mathrm{p}}$ and let $\boldsymbol{\varphi}_k \in \mathbb{C}^{\tau_{\mathrm{p}}\times 1}$ be the pilot sequence belonging to AS_k with $\boldsymbol{\varphi}_k^H\boldsymbol{\varphi}_{k'} = 1,\ \forall k' \in \mathcal{P}_k$, where $\mathcal{P}_k$ denotes the set of ASs that reuse the same pilot as AS_k, including AS_k itself. The random pilot assignment strategy in [21] is advocated to allocate pilots for ASs. After all ASs sending their pilots to the APs, the superimposed pilot signals received at AP_l is expressed as

$$\mathbf{Y}_l = \sqrt{\rho_{\mathrm{p}}\tau_{\mathrm{p}}}\sum_{k'=1}^{K}\mathbf{g}_{lk'}\boldsymbol{\varphi}_{k'}^H + \mathbf{N}_l, \tag{2}$$

where ρ_{p} denotes the training power and $\mathbf{N}_l$ is the additive white Gaussian noise (AWGN) with the t-th column satisfying $[\mathbf{N}_l]_t \sim \mathcal{N}_{\mathbb{C}}\left(\mathbf{0}_N, \sigma^2\mathbf{I}_N\right)$, where σ^2 means the noise variance. Next, AP_l multiplies $\mathbf{Y}_l$ with $\boldsymbol{\varphi}_k$, which de-spreads $\mathbf{Y}_l$ and yields

$$\begin{aligned}\mathbf{y}_{lk} &= \mathbf{Y}_l\boldsymbol{\varphi}_k \\ &= \sqrt{\rho_{\mathrm{p}}\tau_{\mathrm{p}}}\sum_{k'=1}^{K}\mathbf{g}_{lk'}\boldsymbol{\varphi}_{k'}^H\boldsymbol{\varphi}_k + \mathbf{N}_l\boldsymbol{\varphi}_k.\end{aligned} \tag{3}$$

With the knowledge of $\mathbf{y}_{lk}$ and by virtue of the minimum mean square error (MMSE) estimate technique [21]–[23], the MMSE estimate of $\mathbf{g}_{lk}$ is written as

$$\hat{\mathbf{g}}_{lk} = \frac{\mathbb{E}\left\{\mathbf{g}_{lk}^H\mathbf{y}_{lk}\right\}}{\mathbb{E}\left\{\mathbf{y}_{lk}^H\mathbf{y}_{lk}\right\}}\mathbf{y}_{lk} = c_{lk}\mathbf{y}_{lk}, \tag{4}$$

where

$$c_{lk} = \frac{\sqrt{\rho_{\mathrm{p}}\tau_{\mathrm{p}}}\beta_{lk}}{\rho_{\mathrm{p}}\tau_{\mathrm{p}}\sum\limits_{k'=1}^{K}\beta_{lk'}\left|\boldsymbol{\varphi}_{k'}^H\boldsymbol{\varphi}_k\right|^2 + \sigma^2}. \tag{5}$$

In addition, the MMSE channel estimate $\hat{\mathbf{g}}_{lk}$ and the corresponding channel estimate error $\tilde{\mathbf{g}}_{lk} \triangleq \mathbf{g}_{lk} - \hat{\mathbf{g}}_{lk}$ are Gaussian random vectors with the statistics being

$$\hat{\mathbf{g}}_{lk} \sim \mathcal{N}_{\mathbb{C}}\left(\mathbf{0}_N, \gamma_{lk}\mathbf{I}_N\right),\ \tilde{\mathbf{g}}_{lk} \sim \mathcal{N}_{\mathbb{C}}\left(\mathbf{0}_N, \left(\beta_{lk} - \gamma_{lk}\right)\mathbf{I}_N\right), \tag{6}$$

where $\gamma_{lk} = \sqrt{\rho_{\mathrm{p}}\tau_{\mathrm{p}}}c_{lk}\beta_{lk}$.

B. DL Energy Transfer and Information Reception

As mentioned above, the APs perform the SWIPT in this phase based on the TS receiver protocol by dividing DL time-slots into two individual segments: one for energy harvesting while the other for payload information reception. Let s_k, be the data signal intended for AS_k, where $\mathbb{E}\left\{s_k s_{k'}^*\right\} = 1$, if

$k = k'$ and 0 otherwise. Then the signal transmitted from AP_l is written as a unified form for both CB and NCB schemes as follows

$$\mathbf{x}_l = \sqrt{\rho_\mathrm{d}} \sum_{k=1}^{K} \sqrt{\eta_{lk}} \mathbf{w}_{lk} s_k, \tag{7}$$

where ρ_d is the DL transmission power and $\mathbf{w}_{lk}$ denotes the precoding vector used by AP_l in the service of AS_k. In addition, η_{lk} represents the power weighting factor and is designed to satisfy the following transmit power constraint

$$\mathbb{E}\left\{\left\|\mathbf{x}_l\right\|^2\right\} = \rho_\mathrm{d} \sum_{k=1}^{K} \eta_{lk} \mathbb{E}\left\{\left\|\mathbf{w}_{lk}\right\|^2\right\} \leqslant \rho_\mathrm{d}. \tag{8}$$

Note that distinct precoders admit different power weighting factors and we denote these factors associated with CB and NCB schemes as η_{lk}^{CB} and η_{lk}^{NCB}, respectively. As per (7), the signal received at AS_k resulting from the joint coherent transmission by all APs is written as

$$\begin{aligned} \hat{s}_k &= \sum_{l=1}^{L} \mathbf{g}_{lk}^T \mathbf{x}_l \\ &= \sqrt{\rho_\mathrm{d}} \sum_{k'=1}^{K} \sum_{l=1}^{L} \sqrt{\eta_{lk'}} \mathbf{g}_{lk}^T \mathbf{w}_{lk'} s_{k'} + n_k, \end{aligned} \tag{9}$$

where n_k is the AWGN noise satisfying $n_k \sim \mathcal{N}_{\mathbb{C}}\left(0,\ \sigma^2\right)$.

III. Average HE and Achievable Rate Analyses

In this section, the DL average HE and achievable rate in the presence of CB and NCB techniques are respectively investigated. In addition, mathematically tractable closed-form expressions for the above performance metrics are derived.

A. Average HE Analysis

We follow a simple linear power transfer model from [14], [33] and assume that the ASs are able to capture all kinds of RF power but neglecting the noise power since its contribution is quite limited as compared to that of the signal power [34], [35]. With this insight and by virtue of (9), a unified expression for the average HE at AS_k during $\alpha\tau_\mathrm{d}$ channel taps via CB and NCB techniques is formulated as

$$\begin{aligned} \mathcal{E}_k &= \kappa\alpha\tau_\mathrm{d}\rho_\mathrm{d}\mathbb{E}\left\{\left|\sum_{k'=1}^{K}\sum_{l=1}^{L}\sqrt{\eta_{lk'}}\mathbf{g}_{lk}^T\mathbf{w}_{lk'}s_{k'}\right|^2\right\} \\ &= \kappa\alpha\tau_\mathrm{d}\rho_\mathrm{d}\sum_{k'=1}^{K}\mathbb{E}\left\{\left|\sum_{l=1}^{L}\sqrt{\eta_{lk'}}\mathbf{g}_{lk}^T\mathbf{w}_{lk'}\right|^2\right\}, \end{aligned} \tag{10}$$

where $\kappa \in [0,1]$ denotes the RF to direct current (RF-to-DC) conversion efficiency. Recalling that CB and NCB schemes enable $\mathbf{w}_{lk}^{\mathrm{CB}} = \hat{\mathbf{g}}_{lk}^*$ and $\mathbf{w}_{lk}^{\mathrm{NCB}} = \hat{\mathbf{g}}_{lk}^* / \left\|\hat{\mathbf{g}}_{lk}\right\|$, the rigorous closed-form HE expressions of AS_k for any finite L, K, and N are obtained by inserting these settings into (10) and shown in the following Theorem 1.

Theorem 1: The RF energy captured by AS_k with the CB scheme in each coherence interval is written as

$$\mathcal{E}_k^{\mathrm{CB}}\left(\boldsymbol{\xi}\right) = N\kappa\alpha\tau_\mathrm{d}\rho_\mathrm{d}\left(\sum_{k'=1}^{K}\left\|\boldsymbol{\Theta}_k\bar{\boldsymbol{\xi}}_{k'}\right\|^2 + N\sum_{k'=1}^{K}\left(\boldsymbol{\omega}_{k'k}^T\bar{\boldsymbol{\xi}}_{k'}\right)^2\right), \tag{11}$$

where $\boldsymbol{\xi} = \left[\boldsymbol{\xi}_1^T, ..., \boldsymbol{\xi}_L^T\right]^T$, $\boldsymbol{\xi}_l = \left[\xi_{l1}, ..., \xi_{lK}\right]^T$, $\bar{\boldsymbol{\xi}}_k = \left[\xi_{1k}, ..., \xi_{Lk}\right]^T$, $\xi_{lk} = \left(\eta_{lk}^{\mathrm{CB}}\gamma_{lk}\right)^{1/2}$, $\boldsymbol{\Theta}_k = \mathrm{diag}\left(\sqrt{\beta_{1k}}, ..., \sqrt{\beta_{Lk}}\right)$, and $\boldsymbol{\omega}_{k'k} = \left|\boldsymbol{\varphi}_{k'}^H\boldsymbol{\varphi}_k\right|\left[\sqrt{\gamma_{1k}}, ..., \sqrt{\gamma_{Lk}}\right]^T$. In addition, the average HE at AS_k in each coherence interval by resorting to the NCB scheme is equal to[1]

$$\mathcal{E}_k^{\mathrm{NCB}}\left(\boldsymbol{\zeta}\right) = \kappa\alpha\tau_\mathrm{d}\rho_\mathrm{d}\left(\sum_{k'=1}^{K}\left\|\boldsymbol{\Xi}_{k'k}\bar{\boldsymbol{\zeta}}_{k'}\right\|^2 + \Gamma_N^2\sum_{k'=1}^{K}\left(\boldsymbol{\omega}_{k'k}^T\bar{\boldsymbol{\zeta}}_{k'}\right)^2\right), \tag{12}$$

where $\boldsymbol{\zeta} = \left[\boldsymbol{\zeta}_1^T, ..., \boldsymbol{\zeta}_L^T\right]^T$, $\boldsymbol{\zeta}_l = \left[\zeta_{l1}, ..., \zeta_{lK}\right]^T$, $\bar{\boldsymbol{\zeta}}_k = \left[\zeta_{1k}, ..., \zeta_{Lk}\right]^T$, $\zeta_{lk} = \left(\eta_{lk}^{\mathrm{NCB}}\right)^{1/2}$, $\Gamma_N = \Gamma\left(N+1/2\right)/\Gamma\left(N\right)$, and $\boldsymbol{\Xi}_{k'k} = \mathrm{diag}\left(\sqrt{\beta_{1k} + \left(N-1-\Gamma_N^2\right)\left|\boldsymbol{\varphi}_{k'}^H\boldsymbol{\varphi}_k\right|^2\gamma_{lk}}, ..., \sqrt{\beta_{Lk} + \left(N-1-\Gamma_N^2\right)\left|\boldsymbol{\varphi}_{k'}^H\boldsymbol{\varphi}_k\right|^2\gamma_{Lk}}\right)$.

Proof 1: See Appendix A.

The sum-HEs of the considered network with CB and NCB techniques during τ_d channel uses are respectively expressed as $\mathcal{E}_{\mathrm{sum}}^{\mathrm{CB}}\left(\boldsymbol{\xi}\right) \triangleq \sum_{k=1}^{K}\mathcal{E}_k^{\mathrm{CB}}\left(\boldsymbol{\xi}\right)$ and $\mathcal{E}_{\mathrm{sum}}^{\mathrm{NCB}}\left(\boldsymbol{\zeta}\right) \triangleq \sum_{k=1}^{K}\mathcal{E}_k^{\mathrm{NCB}}\left(\boldsymbol{\zeta}\right)$.

Remark 1: From Theorem 1, we have some interesting observations as follows.

1) Since $f_1\left(N\right) = \Gamma_N^2$ behaves as an increasing function with respect to N and $f_2\left(N\right) = N - 1 - \Gamma_N^2$ monotonically decreases as N increases, both $\mathcal{E}_k^{\mathrm{CB}}$ and $\mathcal{E}_k^{\mathrm{NCB}}$ grow with N, which implies that using additional antennas at the APs helps the sensors to reap more RF energy.

2) Focusing on $\mathcal{E}_k^{\mathrm{CB}}$, it is clear that the pilot contamination renders some energy terms in the second summation, but it is insufficient to conclude that the pilot contamination has a positive effect on the energy enhancement because the quality of the channel estimate (i.e., γ_{lk}) is also deteriorated. Besides, it is more difficult to intuitively figure out what role the pilot contamination plays in changing $\mathcal{E}_k^{\mathrm{NCB}}$ since $f_2\left(N\right) = N - 1 - \Gamma_N^2 < 0$ for any natural integer N.

B. Achievable Rate Analysis

Since the sensors lack perfect CSI, they have performed data decoding by only exploiting the knowledge of the channel statistics, which indicates that $\mathbb{E}\left\{\mathbf{g}_{lk}^T\mathbf{w}_{lk}\right\}$ is known in advance and the uncertainty is $\mathbf{g}_{lk}^T\mathbf{w}_{lk} - \mathbb{E}\left\{\mathbf{g}_{lk}^T\mathbf{w}_{lk}\right\}$. With this insight and by virtue of (9), $\hat{s}_k$ can be represented as

$$\hat{s}_k = \sqrt{\rho_\mathrm{d}}\sum_{l=1}^{L}\sqrt{\eta_{lk}}\mathbb{E}\left\{\mathbf{g}_{lk}^T\mathbf{w}_{lk}\right\}s_k + w_k, \tag{13}$$

[1]Note that in Theorem 1, we change the variables from η_{lk}^{CB} to ξ_{lk} for CB technique and η_{lk}^{NCB} to ζ_{lk} for NCB technique to simplify the objective gradient expressions in Sections IV and V.

$$\mathcal{R}_k = (1-\alpha)\log_2\left(1+\frac{\rho_{\rm d}\left|\sum\limits_{l=1}^{L}\sqrt{\eta_{lk}}\mathbb{E}\left\{\mathbf{g}_{lk}^T\mathbf{w}_{lk}\right\}\right|^2}{\rho_{\rm d}{\rm Var}\left(\sum\limits_{l=1}^{L}\sqrt{\eta_{lk}}\mathbf{g}_{lk}^T\mathbf{w}_{lk}\right)+\rho_{\rm d}\sum\limits_{k'\neq k}^{K}\mathbb{E}\left\{\left|\sum\limits_{l=1}^{L}\sqrt{\eta_{lk'}}\mathbf{g}_{lk}^T\mathbf{w}_{lk'}\right|^2\right\}+\sigma^2}\right). \tag{15}$$

where

$$w_k = \sqrt{\rho_{\rm d}}\sum_{l=1}^{L}\sqrt{\eta_{lk}}\left(\mathbf{g}_{lk}^T\mathbf{w}_{lk}-\mathbb{E}\left\{\mathbf{g}_{lk}^T\mathbf{w}_{lk}\right\}\right)s_k + \sqrt{\rho_{\rm d}}\sum_{k'\neq k}^{K}\sum_{l=1}^{L}\sqrt{\eta_{lk'}}\mathbf{g}_{lk}^T\mathbf{w}_{lk'}s_{k'}+n_k. \tag{14}$$

Since n_k is uncorrelated with s_k and data symbols intended for different ASs are uncorrelated, we can conclude that the first summation in (13) is uncorrelated with all interference terms in (14). Then, bearing in mind that uncorrelated Gaussian noise leads to a capacity lower bound [21]–[23], the achievable DL rate expression of AS_k for the precoder $\mathbf{w}_{lk}$ is given as (15), where "Var" denotes the variance operator.

We stress that the achievable rate bound in (15) is valid for any precoding schemes. Same as Theorem 1, we next present rigorous closed-form rate expressions of AS_k for any finite L, K, and N with CB and NCB schemes by calculating all expectation terms in (15).

Theorem 2: Assuming only channel statistics are available at the ASs, an achievable rate expression of AS_k with the CB technique is given as

$$\mathcal{R}_k^{\rm CB}(\boldsymbol{\xi}) = (1-\alpha)\times \log_2\left(1+\frac{N^2\rho_{\rm d}\left(\boldsymbol{\omega}_{kk}^T\bar{\boldsymbol{\xi}}_k\right)^2}{N^2\rho_{\rm d}\sum\limits_{k'\neq k}^{K}\left(\boldsymbol{\omega}_{k'k}^T\bar{\boldsymbol{\xi}}_{k'}\right)^2+N\rho_{\rm d}\sum\limits_{k'=1}^{K}\left\|\boldsymbol{\Theta}_k\bar{\boldsymbol{\xi}}_{k'}\right\|^2+\sigma^2}\right). \tag{16}$$

Besides, when considering the NCB technique, an achievable rate expression of AS_k is written as

$$\mathcal{R}_k^{\rm NCB}(\boldsymbol{\zeta}) = (1-\alpha)\times \log_2\left(1+\frac{\Gamma_N^2\rho_{\rm d}\left(\boldsymbol{\omega}_{kk}^T\bar{\boldsymbol{\zeta}}_k\right)^2}{\Gamma_N^2\rho_{\rm d}\sum\limits_{k'\neq k}^{K}\left(\boldsymbol{\omega}_{k'k}^T\bar{\boldsymbol{\zeta}}_{k'}\right)^2+\rho_{\rm d}\sum\limits_{k'=1}^{K}\left\|\boldsymbol{\Xi}_{k'k}\bar{\boldsymbol{\zeta}}_{k'}\right\|^2+\sigma^2}\right). \tag{17}$$

Proof 2: See Appendix B.

The sum-rates of the considered network with CB and NCB techniques are respectively expressed as $\mathcal{R}_{\rm sum}^{\rm CB}(\boldsymbol{\xi}) \triangleq \sum_{k=1}^{K}\mathcal{R}_k^{\rm CB}(\boldsymbol{\xi})$ and $\mathcal{R}_{\rm sum}^{\rm NCB}(\boldsymbol{\zeta}) \triangleq \sum_{k=1}^{K}\mathcal{R}_k^{\rm NCB}(\boldsymbol{\zeta})$.

Remark 2: Based on the closed-form rate expressions established in Theorem 2, we obtain the following insights.

1) Since a larger AP antenna number admits more array gains and degree of freedoms, equipping the APs with more antennas always improves the achievable rate. This finding is in accordance with the first observation in Remark 1.

2) There is no doubt that a higher $\mathcal{R}_k$ will be approached by reserving more time-slots for information reception, i.e., a lower α, but it inevitably decreases $\mathcal{E}_k$. Since different precoders yield different $\mathcal{E}_k$ and $\mathcal{R}_k$, it is much interesting to explore how the precoders affect the HE-rate trade-offs. In Section IV, we will numerically investigate these trade-offs by traveling the closed-form HE and rate expressions in Theorems 1 and 2 under variable TS factors and different power control strategies.

IV. APG-based Max-Min Fairness Power Control for Average HE

In this section, to tackle the severe HE discrepancy issue that arises from the great range of large-scale fading coefficients between APs and sensors, the APG-based max-min HE power control policies under CB and NCB schemes are presented, which can ensure the maximized identical HE for all ASs.

Mathematically, the max-min HE power optimization problem under a set of per-AP power constraints is formulated as

$$\mathbb{H}: \max_{\{\eta_{lk}\}}\ \min_{\forall k}\ \mathcal{E}_k \tag{18a}$$

$$\text{s.t.}\ \sum_{k=1}^{K}\eta_{lk}\mathbb{E}\left\{\left\|\mathbf{w}_{lk}\right\|^2\right\}\leqslant 1, \forall l, \tag{18b}$$

where $\mathcal{E}_k$ is defined in (10). Note that problem $\mathbb{H}$ is valid for both CB and NCB schemes. In the following, we first detail a rigorous formulation of the considered problem with the CB scheme.

A. Max-Min HE for CB Scheme

By inserting $\mathbf{w}_{lk}^{\rm CB} = \hat{\mathbf{g}}_{lk}^*$ into problem $\mathbb{H}$, we obtain

$$\mathbb{H}^{\rm CB}: \max\ f(\boldsymbol{\xi}) \triangleq \min_{\forall k}\mathcal{E}_k^{\rm CB}(\boldsymbol{\xi}) \tag{19a}$$

$$\text{s.t.}\ \boldsymbol{\xi}\in\mathcal{S} = \left\{\boldsymbol{\xi}|\xi_{lk}\geqslant 0; \|\boldsymbol{\xi}_l\|\leqslant 1/\sqrt{N}, \forall l, \forall k\right\}, \tag{19b}$$

where $\mathcal{E}_k^{\rm CB}(\boldsymbol{\xi})$ is exhibited in (11) and $\mathcal{S}$ denotes the feasible set of $\boldsymbol{\xi}$. It remarks that the objective function $f(\boldsymbol{\xi})$ is non-differentiable with respect to $\boldsymbol{\xi}$ and the APG method cannot be directly employed to solve problem $\mathbb{H}^{\rm CB}$ [30]–[32]. Fortunately, a smoothing technique can be utilized to tackle this issue by recalling a log-sum-exp function [36]

$$f(\boldsymbol{\xi},\lambda) = -\frac{1}{\lambda}\ln\left(\frac{1}{K}\sum_{k=1}^{K}e^{-\lambda\mathcal{E}_k^{\rm CB}(\boldsymbol{\xi})}\right), \tag{20}$$

where $\lambda>0$ represents the smoothness parameter. Note that $f(\boldsymbol{\xi},\lambda)$ is a differentiable approximation of $f(\boldsymbol{\xi})$ with an accuracy of $\log K/\lambda$ [36]. As per (20), an approximate solution

Algorithm 1 The APG-based algorithm for solving $\mathbb{H}^{\text{CB}}$

Input: $\boldsymbol{\xi}^{(0)} \in \mathcal{S}$, $\rho^{(0)} = \rho^{(1)} = 1$, $0 < \upsilon < 1/\mathcal{L}_f$, $\lambda > 0$, $\mathcal{I}$;
Output: $\boldsymbol{\xi}^{\text{Opt}}$.

Set $i = 1$. Let $\boldsymbol{\xi}^{(1)} = \boldsymbol{\psi}^{(1)} = \boldsymbol{\xi}^{(0)}$;
while $i \leqslant \mathcal{I}$ **do**
  $\boldsymbol{\theta}^{(i)} = \boldsymbol{\xi}^{(i)} + \frac{\rho^{(i-1)}}{\rho^{(i)}}\left(\boldsymbol{\psi}^{(i)} - \boldsymbol{\xi}^{(i)}\right) + \left(\boldsymbol{\xi}^{(i)} - \boldsymbol{\xi}^{(i-1)}\right) \times \frac{\rho^{(i-1)}-1}{\rho^{(i)}}$;
  $\boldsymbol{\psi}^{(i+1)} = P_{\mathcal{S}}\left(\boldsymbol{\theta}^{(i)} + \upsilon \nabla f\left(\boldsymbol{\theta}^{(i)}, \lambda\right)\right)$;
  $\boldsymbol{\phi}^{(i+1)} = P_{\mathcal{S}}\left(\boldsymbol{\xi}^{(i)} + \upsilon \nabla f\left(\boldsymbol{\xi}^{(i)}, \lambda\right)\right)$;
  $\boldsymbol{\xi}^{(i+1)} = \begin{cases} \boldsymbol{\psi}^{(i+1)}, \text{ if } f\left(\boldsymbol{\psi}^{(i+1)}\right) \geqslant f\left(\boldsymbol{\phi}^{(i+1)}\right) \\ \boldsymbol{\phi}^{(i+1)}, \text{ otherwise} \end{cases}$;
  $\rho^{(i+1)} = \left(\sqrt{4\left(\rho^{(i)}\right)^2 + 1} + 1\right)/2$;
  Reset $i := i + 1$;
end while
Let $\boldsymbol{\xi}^{\text{Opt}} = \boldsymbol{\xi}^{(i)}$.

to $\mathbb{H}^{\text{CB}}$ can be determined by implementing the monotone APG method [30]–[32] outlined in Algorithm 1, provided that a sufficiently large λ is available. We detail this algorithm at the top of the next page and denote the corresponding optimal HE for the CB scheme as $\mathcal{E}^{\text{CB-Opt}} \triangleq f\left(\boldsymbol{\xi}^{\text{Opt}}\right)$, where $\boldsymbol{\xi}^{\text{Opt}}$ is the optimal solution to $\mathbb{H}^{\text{CB}}$.

In Algorithm 1, the superscripts indicate the iteration numbers, $\boldsymbol{\xi}^{(0)} \in \mathcal{S}$ is the initial solution, $\mathcal{I}$ denotes the maximum number of iterations, and υ corresponds to the step length, which is required to be smaller than $1/\mathcal{L}_f$ to guarantee convergence, where $\mathcal{L}_f$ refers to the Lipschitz constant of the gradient of $f(\boldsymbol{\xi}, \lambda)$, $\nabla f(\boldsymbol{\xi}, \lambda)$. Besides, $P_{\mathcal{S}}(\boldsymbol{\xi})$ represents the projection onto the feasible set $\mathcal{S}$. In what follows, we will separately detail the operators $\nabla f(\boldsymbol{\xi}, \lambda)$ and $P_{\mathcal{S}}(\boldsymbol{\xi})$.

1) The gradient of $f(\boldsymbol{\xi}, \lambda)$: Since the gradient of a multivariable function can be written as a vector of all its partial derivatives, which yields

$$\nabla f(\boldsymbol{\xi}, \lambda) = \left[\frac{\partial}{\partial \boldsymbol{\xi}_1} f(\boldsymbol{\xi}, \lambda), \frac{\partial}{\partial \boldsymbol{\xi}_2} f(\boldsymbol{\xi}, \lambda), ..., \frac{\partial}{\partial \boldsymbol{\xi}_K} f(\boldsymbol{\xi}, \lambda)\right]^T, \tag{21}$$

where

$$\frac{\partial}{\partial \bar{\boldsymbol{\xi}}_{k'}} f(\boldsymbol{\xi}, \lambda) = \frac{\sum_{k=1}^{K} e^{-\lambda \mathcal{E}_k^{\text{CB}}(\boldsymbol{\xi})} \times \frac{\partial}{\partial \bar{\boldsymbol{\xi}}_{k'}} \mathcal{E}_k^{\text{CB}}(\boldsymbol{\xi})}{\sum_{k=1}^{K} e^{-\lambda \mathcal{E}_k^{\text{CB}}(\boldsymbol{\xi})}}. \tag{22}$$

Using the equality $\nabla \|\mathbf{A}\mathbf{x}\|^2 = 2\mathbf{A}^T\mathbf{A}\mathbf{x}$ for any symmetric matrix $\mathbf{A}$, $\frac{\partial}{\partial \bar{\boldsymbol{\xi}}_{k'}} \mathcal{E}_k^{\text{CB}}(\boldsymbol{\xi})$ is computed as

$$\frac{\partial}{\partial \bar{\boldsymbol{\xi}}_{k'}} \mathcal{E}_k^{\text{CB}}(\boldsymbol{\xi}) = 2N\kappa\alpha\tau_{\text{d}}\rho_{\text{d}}\left(\boldsymbol{\Theta}_k^2 \bar{\boldsymbol{\xi}}_{k'} + N\boldsymbol{\omega}_{k'k}\boldsymbol{\omega}_{k'k}^T \bar{\boldsymbol{\xi}}_{k'}\right). \tag{23}$$

2) Projection onto $\mathcal{S}$: In fact, the projection onto $\mathcal{S}$ admits a mathematical closed-form solution. Specifically, for a given vector $\mathbf{x} = \left[\mathbf{x}_1^T, ..., \mathbf{x}_L^T\right]^T$ with $\mathbf{x}_l \in \mathbb{C}^{N\times 1}$, $P_{\mathcal{S}}(\mathbf{x})$ is the solution to the following minimization problem

$$\min_{\boldsymbol{\xi}} \left\{\|\boldsymbol{\xi} - \mathbf{x}\|^2 | \boldsymbol{\xi} \in \mathcal{S}\right\}. \tag{24}$$

Since $\|\boldsymbol{\xi} - \mathbf{x}\|^2$ is separable with respect to $\boldsymbol{\xi}_l$, problem (24) can be decomposed into a series of sub-problems for each AP as

$$\min_{\boldsymbol{\xi}_l} \left\{\|\boldsymbol{\xi}_l - \mathbf{x}_l\|^2 | \xi_{lk} \geqslant 0; \|\boldsymbol{\xi}_l\| \leqslant 1/\sqrt{N}, \forall l, \forall k\right\}, \tag{25}$$

which corresponds to the projection onto the intersection of the positive orthant and a Euclidean ball. By virtue of [37, Theorem 7.1], the solution to (25) is found as

$$\boldsymbol{\xi}_l = \frac{1/\sqrt{N}}{\max\left(1/\sqrt{N}, \left\|[\mathbf{x}_l]_+\right\|\right)}[\mathbf{x}_l]_+, \tag{26}$$

where notation $[\mathbf{x}_l]_+$ means the projection onto the positive orthant. By stacking the results in (26) associated with all APs into a vector, the solution to (24) is obtained.

B. Max-Min HE for NCB Scheme

Likewise, when concentrating on NCB scheme, problem $\mathbb{H}^{\text{NCB}}$ can be specified by inserting $\mathbf{w}_{lk}^{\text{NCB}} = \hat{\mathbf{g}}_{lk}^* / \|\hat{\mathbf{g}}_{lk}\|$ into problem $\mathbb{H}$

$$\mathbb{H}^{\text{NCB}}: \max \ \bar{f}(\boldsymbol{\zeta}) \triangleq \min_{\forall k} \mathcal{E}_k^{\text{NCB}}(\boldsymbol{\zeta}) \tag{27a}$$

$$\text{s.t. } \boldsymbol{\zeta} \in \bar{\mathcal{S}} = \left\{\boldsymbol{\zeta} | \zeta_{lk} \geqslant 0; \|\boldsymbol{\zeta}_l\| \leqslant 1, \forall l, \forall k\right\}, \tag{27b}$$

where $\mathcal{E}_k^{\text{NCB}}(\boldsymbol{\zeta})$ is listed in (12) and $\bar{\mathcal{S}}$ denotes the feasible set of $\boldsymbol{\zeta}$. Same as $\mathbb{H}^{\text{CB}}$, an approximate solution to $\mathbb{H}^{\text{NCB}}$ can be approached by implementing Algorithm 1 with $\boldsymbol{\xi}$, $\mathcal{S}$, and $f(\boldsymbol{\xi}, \lambda)$ being respectively substituted with $\boldsymbol{\zeta}$, $\bar{\mathcal{S}}$, and $\bar{f}(\boldsymbol{\zeta}, \lambda)$, where

$$\bar{f}(\boldsymbol{\zeta}, \lambda) = -\frac{1}{\lambda} \ln\left(\frac{1}{K}\sum_{k=1}^{K} e^{-\lambda \mathcal{E}_k^{\text{NCB}}(\boldsymbol{\zeta})}\right). \tag{28}$$

Let the corresponding optimal HE for the NCB scheme be $\mathcal{E}^{\text{NCB-Opt}} \triangleq \bar{f}\left(\boldsymbol{\zeta}^{\text{Opt}}\right)$, where $\boldsymbol{\zeta}^{\text{Opt}}$ is the optimal solution to $\mathbb{H}^{\text{NCB}}$. Based upon (28), the gradient of $\bar{f}(\boldsymbol{\zeta}, \lambda)$ is expressed as

$$\nabla \bar{f}(\boldsymbol{\zeta}, \lambda) = \left[\frac{\partial}{\partial \bar{\boldsymbol{\zeta}}_1} \bar{f}(\boldsymbol{\zeta}, \lambda), \frac{\partial}{\partial \bar{\boldsymbol{\zeta}}_2} \bar{f}(\boldsymbol{\zeta}, \lambda), ..., \frac{\partial}{\partial \bar{\boldsymbol{\zeta}}_K} \bar{f}(\boldsymbol{\zeta}, \lambda)\right]^T, \tag{29}$$

where

$$\frac{\partial}{\partial \bar{\boldsymbol{\zeta}}_{k'}} f(\boldsymbol{\zeta}, \lambda) = \frac{\sum_{k=1}^{K} e^{-\lambda \mathcal{E}_k^{\text{NCB}}(\boldsymbol{\zeta})} \times \frac{\partial}{\partial \bar{\boldsymbol{\zeta}}_{k'}} \mathcal{E}_k^{\text{NCB}}(\boldsymbol{\zeta})}{\sum_{k=1}^{K} e^{-\lambda \mathcal{E}_k^{\text{NCB}}(\boldsymbol{\zeta})}}, \tag{30}$$

and

$$\frac{\partial}{\partial \bar{\boldsymbol{\zeta}}_{k'}} \mathcal{E}_k^{\text{NCB}}(\boldsymbol{\zeta}) = 2\kappa\alpha\tau_{\text{d}}\rho_{\text{d}}\left(\Xi_k^2 \bar{\boldsymbol{\zeta}}_{k'} + \Gamma_N^2 \boldsymbol{\omega}_{k'k}\boldsymbol{\omega}_{k'k}^T \bar{\boldsymbol{\zeta}}_{k'}\right). \tag{31}$$

In addition, the projection onto $\bar{\mathcal{S}}$ yields

$$\boldsymbol{\zeta}_l = \frac{1}{\max\left(1, \left\|[\mathbf{x}_l]_+\right\|\right)}[\mathbf{x}_l]_+. \tag{32}$$

C. Complexity Analysis

Focusing on problem $\mathbb{H}^{\text{CB}}$, it is easy to conclude that the computational complexity of each iteration in Algorithm 1 mainly lies in three arithmetic operators: $f(\boldsymbol{\xi})$, $\nabla f(\boldsymbol{\xi},\lambda)$, and $P_{\mathcal{S}}(\boldsymbol{\xi})$. Since calculating $\mathcal{E}_k^{\text{CB}}(\boldsymbol{\xi})$ requires LK multiplications, the complexities of finding $f(\boldsymbol{\xi})$ and $\nabla f(\boldsymbol{\xi},\lambda)$ are both $\mathcal{O}\left(LK^2\right)$. Besides, the complexity of $P_{\mathcal{S}}(\boldsymbol{\xi})$ is $\mathcal{O}(LK)$. In conclusion, the complexity of each iteration in Algorithm 1 for determining $\mathbb{H}^{\text{CB}}$ is $\mathcal{O}\left(LK^2\right)$. Likewise, the per-iteration complexity for determining $\mathbb{H}^{\text{NCB}}$ is also $\mathcal{O}\left(LK^2\right)$.

V. APG-based Max-Min Fairness Power Control for Achievable Rate

In this section, we aim to design the max-min fairness power control strategies for the DL achievable rate under both CB and NCB techniques and determine the optimums $\mathcal{R}^{\text{CB-Opt}}$ and $\mathcal{R}^{\text{NCB-Opt}}$ by applying the APG method. These obtained optimums combined with $\mathcal{E}^{\text{CB-Opt}}$ and $\mathcal{E}^{\text{NCB-Opt}}$ derived in Section IV facilitate quantifying the max-min HE-rate trade-offs under different precoding schemes.

A. Max-Min Achievable Rate for CB Scheme

The max-min fairness power control problem with respect to the achievable rate under a set of per-AP power constraints for the CB scheme has the form of

$$\mathbb{R}^{\text{CB}}: \max\ \mathcal{M}(\boldsymbol{\xi}) \triangleq \min_{\forall k} \mathcal{R}_k^{\text{CB}}(\boldsymbol{\xi}) \tag{33a}$$

$$\text{s.t. } \boldsymbol{\xi} \in \mathcal{S}, \tag{33b}$$

where $\mathcal{R}_k^{\text{CB}}(\boldsymbol{\xi})$ and $\mathcal{S}$ are defined in (16) and (19b), respectively. It remarks that $\mathcal{M}(\boldsymbol{\xi})$ is also non-differentiable with respect to $\boldsymbol{\xi}$ and the smoothing method [36] discussed in the former section should be recalled. With this technique, an approximate solution to problem $\mathbb{R}^{\text{CB}}$ can be determined by resorting to Algorithm 1 with $f(\boldsymbol{\xi},\lambda)$ being replaced with $\mathcal{M}(\boldsymbol{\xi},\lambda)$, where

$$\mathcal{M}(\boldsymbol{\xi},\lambda) = -\frac{1}{\lambda}\ln\left(\frac{1}{K}\sum_{k=1}^{K} e^{-\lambda \mathcal{R}_k^{\text{CB}}(\boldsymbol{\xi})}\right). \tag{34}$$

The resulting optimal achievable rate with the CB scheme is denoted as $\mathcal{R}^{\text{CB-Opt}} \triangleq \mathcal{M}\left(\boldsymbol{\xi}^{\text{Opt}}\right)$, where $\boldsymbol{\xi}^{\text{Opt}}$ corresponds to the optimal solution to $\mathbb{R}^{\text{CB}}$. Note that the difference between problems $\mathbb{H}^{\text{CB}}$ and $\mathbb{R}^{\text{CB}}$ manifests itself in the objectives, we only need to recalculate the gradient of $\mathcal{M}(\boldsymbol{\xi},\lambda)$, $\nabla\mathcal{M}(\boldsymbol{\xi},\lambda)$. It is expressed as

$$\nabla\mathcal{M}(\boldsymbol{\xi},\lambda) = \left[\tfrac{\partial}{\partial\bar{\boldsymbol{\xi}}_1}\mathcal{M}(\boldsymbol{\xi},\lambda), \tfrac{\partial}{\partial\bar{\boldsymbol{\xi}}_2}\mathcal{M}(\boldsymbol{\xi},\lambda), ..., \tfrac{\partial}{\partial\bar{\boldsymbol{\xi}}_K}\mathcal{M}(\boldsymbol{\xi},\lambda)\right]^T. \tag{35}$$

Let us define $\mathcal{A}_k(\boldsymbol{\xi}) = N^2\rho_{\text{d}}\left(\boldsymbol{\omega}_{kk}^T\bar{\boldsymbol{\xi}}_k\right)^2$ and $\mathcal{B}_k(\boldsymbol{\xi}) = N^2\rho_{\text{d}}\sum\limits_{k'\neq k}^{K}\left(\boldsymbol{\omega}_{k'k}^T\bar{\boldsymbol{\xi}}_{k'}\right)^2 + N\rho_{\text{d}}\sum\limits_{k'=1}^{K}\left\|\boldsymbol{\Theta}_k\bar{\boldsymbol{\xi}}_{k'}\right\|^2 + \sigma^2$, then $\mathcal{R}_k^{\text{CB}}(\boldsymbol{\xi}) = \frac{(1-\alpha)}{\ln 2}\times\left(\ln\left(\mathcal{A}_k(\boldsymbol{\xi})+\mathcal{B}_k(\boldsymbol{\xi})\right) - \ln\left(\mathcal{B}_k(\boldsymbol{\xi})\right)\right)$. By leveraging $\nabla\|\mathbf{A}\mathbf{x}\|^2 = 2\mathbf{A}^T\mathbf{A}\mathbf{x}$, the quantity $\frac{\partial}{\partial\bar{\boldsymbol{\xi}}_{k'}}\mathcal{M}(\boldsymbol{\xi},\lambda)$ in (35) equals

$$\tfrac{\partial}{\partial\bar{\boldsymbol{\xi}}_{k'}}\mathcal{M}(\boldsymbol{\xi},\lambda) = \frac{\sum\limits_{k=1}^{K} e^{-\lambda\mathcal{R}_k^{\text{CB}}(\boldsymbol{\xi})}\times\tfrac{\partial}{\partial\bar{\boldsymbol{\xi}}_{k'}}\mathcal{R}_k^{\text{CB}}(\boldsymbol{\xi})}{\sum\limits_{k=1}^{K} e^{-\lambda\mathcal{R}_k^{\text{CB}}(\boldsymbol{\xi})}}, \tag{36}$$

where

$$\tfrac{\partial}{\partial\bar{\boldsymbol{\xi}}_{k'}}\mathcal{R}_k^{\text{CB}}(\boldsymbol{\xi}) = \frac{(1-\alpha)}{\ln 2}\left(\frac{\tfrac{\partial}{\partial\bar{\boldsymbol{\xi}}_{k'}}\mathcal{A}_k(\boldsymbol{\xi}) + \tfrac{\partial}{\partial\bar{\boldsymbol{\xi}}_{k'}}\mathcal{B}_k(\boldsymbol{\xi})}{\mathcal{A}_k(\boldsymbol{\xi})+\mathcal{B}_k(\boldsymbol{\xi})} - \frac{\tfrac{\partial}{\partial\bar{\boldsymbol{\xi}}_{k'}}\mathcal{B}_k(\boldsymbol{\xi})}{\mathcal{B}_k(\boldsymbol{\xi})}\right), \tag{37}$$

$$\tfrac{\partial}{\partial\bar{\boldsymbol{\xi}}_{k'}}\mathcal{A}_k(\boldsymbol{\xi}) = \begin{cases} 2N^2\rho_{\text{d}}\boldsymbol{\omega}_{kk}\boldsymbol{\omega}_{kk}^T\bar{\boldsymbol{\xi}}_k, \ \forall k'=k, \\ 0, \ \forall k'\neq k, \end{cases} \tag{38}$$

and

$$\tfrac{\partial}{\partial\bar{\boldsymbol{\xi}}_{k'}}\mathcal{B}_k(\boldsymbol{\xi}) = \begin{cases} 2N\rho_{\text{d}}\boldsymbol{\Theta}_k^2\bar{\boldsymbol{\xi}}_k, \ \forall k'=k, \\ 2N^2\rho_{\text{d}}\boldsymbol{\omega}_{k'k}\boldsymbol{\omega}_{k'k}^T\bar{\boldsymbol{\xi}}_{k'} + 2N\rho_{\text{d}}\boldsymbol{\Theta}_k^2\bar{\boldsymbol{\xi}}_{k'}, \ \forall k'\neq k. \end{cases} \tag{39}$$

B. Max-Min Achievable Rate for NCB Scheme

The max-min fairness power control problem for the achievable rate under a set of per-AP power constraints in the presence of the NCB scheme is formulated as

$$\mathbb{R}^{\text{NCB}}: \max\ \bar{\mathcal{M}}(\boldsymbol{\zeta}) \triangleq \min_{\forall k} \mathcal{R}_k^{\text{NCB}}(\boldsymbol{\zeta}) \tag{40a}$$

$$\text{s.t. } \boldsymbol{\zeta} \in \bar{\mathcal{S}}, \tag{40b}$$

where $\mathcal{R}_k^{\text{NCB}}(\boldsymbol{\zeta})$ and $\bar{\mathcal{S}}$ are defined in (17) and (27b), respectively. Following the same techniques for solving problem $\mathbb{H}^{\text{CB}}$, an approximate solution to problem $\mathbb{R}^{\text{NCB}}$ can be approached by implementing Algorithm 1 with $\boldsymbol{\xi}$, $\mathcal{S}$, and $f(\boldsymbol{\xi},\lambda)$ being replaced with $\boldsymbol{\zeta}$, $\bar{\mathcal{S}}$, and $\bar{\mathcal{M}}(\boldsymbol{\zeta},\lambda)$, where

$$\bar{\mathcal{M}}(\boldsymbol{\zeta},\lambda) = -\frac{1}{\lambda}\ln\left(\frac{1}{K}\sum_{k=1}^{K} e^{-\lambda\mathcal{R}_k^{\text{NCB}}(\boldsymbol{\zeta})}\right). \tag{41}$$

The corresponding optimal achievable rate for the NCB scheme is denoted as $\mathcal{R}^{\text{NCB-Opt}} \triangleq \bar{\mathcal{M}}\left(\boldsymbol{\zeta}^{\text{Opt}}\right)$, where $\boldsymbol{\zeta}^{\text{Opt}}$ is the optimal solution to $\mathbb{R}^{\text{NCB}}$. By virtue of (41), the gradient of $\bar{\mathcal{M}}(\boldsymbol{\zeta},\lambda)$ is written as

$$\nabla\bar{\mathcal{M}}(\boldsymbol{\zeta},\lambda) = \left[\tfrac{\partial}{\partial\bar{\boldsymbol{\zeta}}_1}\bar{\mathcal{M}}(\boldsymbol{\zeta},\lambda), \tfrac{\partial}{\partial\bar{\boldsymbol{\zeta}}_2}\bar{\mathcal{M}}(\boldsymbol{\zeta},\lambda), ..., \tfrac{\partial}{\partial\bar{\boldsymbol{\zeta}}_K}\bar{\mathcal{M}}(\boldsymbol{\zeta},\lambda)\right]^T, \tag{42}$$

where

$$\bar{\mathcal{M}}(\boldsymbol{\zeta},\lambda) = -\frac{1}{\lambda}\ln\left(\frac{1}{K}\sum_{k=1}^{K} e^{-\lambda\mathcal{R}_k^{\text{NCB}}(\boldsymbol{\zeta})}\right). \tag{43}$$

Next, using the preliminaries $\mathcal{C}_k(\boldsymbol{\zeta}) = \Gamma_N^2\rho_{\text{d}}\left(\boldsymbol{\omega}_{kk}^T\bar{\boldsymbol{\zeta}}_k\right)^2$ and $\mathcal{D}_k(\boldsymbol{\zeta}) = \Gamma_N^2\rho_{\text{d}}\sum\limits_{k'\neq k}^{K}\left(\boldsymbol{\omega}_{k'k}^T\bar{\boldsymbol{\zeta}}_{k'}\right)^2 + \rho_{\text{d}}\sum\limits_{k'=1}^{K}\left\|\boldsymbol{\Xi}_{k'k}\bar{\boldsymbol{\zeta}}_{k'}\right\|^2 + \sigma^2$, we

obtain $\mathcal{R}_k^{\mathrm{NCB}}(\boldsymbol{\zeta}) = \frac{(1-\alpha)}{\ln 2}\left(\ln\left(\mathcal{C}_k(\boldsymbol{\zeta})+\mathcal{D}_k(\boldsymbol{\zeta})\right)-\ln\left(\mathcal{D}_k(\boldsymbol{\zeta})\right)\right)$. Besides, $\frac{\partial}{\partial \bar{\boldsymbol{\zeta}}_{k'}}\mathcal{R}_k^{\mathrm{NCB}}(\boldsymbol{\zeta})$ equals

$$\frac{\partial}{\partial \bar{\boldsymbol{\zeta}}_{k'}}\mathcal{R}_k^{\mathrm{NCB}}(\boldsymbol{\zeta}) = \frac{(1-\alpha)}{\ln 2}\left(\frac{\frac{\partial}{\partial \bar{\boldsymbol{\zeta}}_{k'}}\mathcal{C}_k(\boldsymbol{\zeta})+\frac{\partial}{\partial \bar{\boldsymbol{\zeta}}_{k'}}\mathcal{D}_k(\boldsymbol{\zeta})}{\mathcal{C}_k(\boldsymbol{\zeta})+\mathcal{D}_k(\boldsymbol{\zeta})}-\frac{\frac{\partial}{\partial \bar{\boldsymbol{\zeta}}_{k'}}\mathcal{D}_k(\boldsymbol{\zeta})}{\mathcal{D}_k(\boldsymbol{\zeta})}\right), \tag{44}$$

where

$$\frac{\partial}{\partial \bar{\boldsymbol{\zeta}}_{k'}}\mathcal{C}_k(\boldsymbol{\zeta}) = \begin{cases} 2\Gamma_N^2\rho_{\mathrm{d}}\boldsymbol{\omega}_{kk}\boldsymbol{\omega}_{kk}^T\bar{\boldsymbol{\zeta}}_k, \ \forall k'=k, \\ 0, \ \forall k'\neq k, \end{cases} \tag{45}$$

and

$$\frac{\partial}{\partial \bar{\boldsymbol{\zeta}}_{k'}}\mathcal{D}_k(\boldsymbol{\zeta}) = \begin{cases} 2\rho_{\mathrm{d}}\boldsymbol{\Xi}_{kk}^2\bar{\boldsymbol{\zeta}}_k, \ \forall k'=k, \\ 2\Gamma_N^2\rho_{\mathrm{d}}\boldsymbol{\omega}_{k'k}\boldsymbol{\omega}_{k'k}^T\bar{\boldsymbol{\zeta}}_{k'}+2\rho_{\mathrm{d}}\boldsymbol{\Xi}_{k'k}^2\bar{\boldsymbol{\zeta}}_{k'}, \ \forall k'\neq k. \end{cases} \tag{46}$$

C. Complexity Analysis

Since the calculations of $\mathcal{R}_k^{\mathrm{CB}}(\boldsymbol{\xi})$ and $\mathcal{R}_k^{\mathrm{NCB}}(\boldsymbol{\zeta})$ both require LK multiplications and the computational complexity of each iteration in Algorithm 1 mainly lies in the objective, gradient, and the projection on the feasible set, the complexity of each iteration for solving $\mathbb{R}^{\mathrm{CB}}$ and $\mathbb{R}^{\mathrm{NCB}}$ is $\mathcal{O}\left(LK^2\right)$.

VI. Simulation Results and Discussions

In this section, extended numerical experiments are presented to compare the CB and NCB techniques in terms of the HE and achievable rate under the full power control (FPC) and APG-based max-min fairness power control strategies. Also, the simulation parameters and system settings are discussed.

A. Parameters Settings

In this work, all APs and sensors are randomly distributed in a square area with side length of 1 km. We adopt the simple FPC as the power control scheme unless power is optimized using our proposed Algorithm 1. Specifically, it admits the power weighting factors as $\eta_{lk}^{\mathrm{CB}} = 1/\left(N\sum_{k'=1}^{K}\gamma_{lk'}\right)$ and $\eta_{lk}^{\mathrm{NCB}} = \gamma_{lk}/\sum_{k'=1}^{K}\gamma_{lk'}, \forall l, \forall k$. Unless otherwise specified, the simulation parameters used in this paper are enumerated in Table II, shown at the top of this page. These parameters are taken from [21].

B. Performance Evaluation

In Fig. 3, the sum-HEs $\mathcal{E}_{\mathrm{sum}}^{\mathrm{CB}}$ and $\mathcal{E}_{\mathrm{sum}}^{\mathrm{NCB}}$ are displayed as the functions of the AS number K for different per-AP antenna number N under the FPC strategy. From Fig. 3, the first observation is that $\mathcal{E}_{\mathrm{sum}}^{\mathrm{CB}}$ substantially outperforms $\mathcal{E}_{\mathrm{sum}}^{\mathrm{NCB}}$ for K ranging from 20 to 200, which means that the CB scheme is able to reap more wireless RF energy than the NCB scheme. Besides, since using additional antennas at the APs harvests more multiplexing and antenna array gains, the sum-HEs related to "$N = 4$" surpass the sum-HEs associated with "$N = 2$", which indicates that increasing N is beneficial for energy harvesting enhancement. Note that in Fig. 3, the curves labeled "$L = 10$" correspond to a traditional distributed mMIMO system with 10 BSs. Given the total antenna number (i.e., LN is fixed), the CF architecture possesses more HE than the distributed counterpart does, which can be explained as the former helps shorten the end-to-end communication distances, thereby alleviating the impact of attenuation. We stress that for both CF and distributed mMIMO topologies, the simulation HE curves are plotted via Monte-Carlo simulations by inserting $\mathbf{w}_{lk}^{\mathrm{CB}} = \hat{\mathbf{g}}_{lk}^*$ and $\mathbf{w}_{lk}^{\mathrm{NCB}} = \hat{\mathbf{g}}_{lk}^*/\|\hat{\mathbf{g}}_{lk}\|$ into (10), and the analytical HE curves are obtained by resorting to (11) and (12), respectively. Fig. 3 shows that the simulated HEs perfectly match the analytical ones, which clearly verifies the tightness of the derived HE expressions in Theorem 1.

TABLE II
System Parameters

Parameter	Value
Noise variance σ^2	-96 dBm
Bandwidth B	20 MHz
Shadow fading standard deviation σ_{sh}	8 dB
Reference distances in (2) $d_0,\ d_1$	0.01, 0.05 km
Length of UL training τ_{p}	20
Length of coherence interval τ_{c}	200
UL training power ρ_{p}	0.5 W
DL transmission power ρ_{d}	1 W
TS factor α	0.4
RF-to-DC conversion efficiency κ	0.8

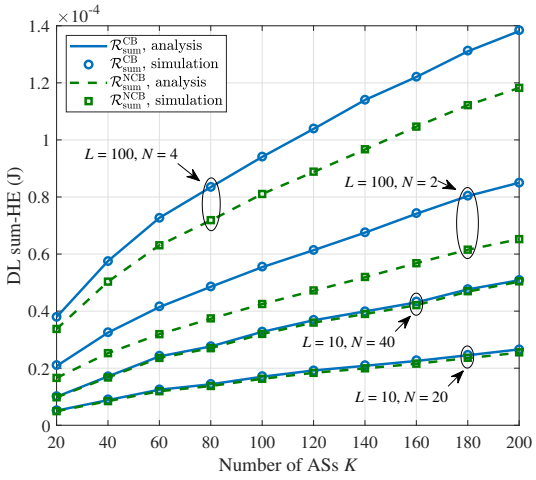

Fig. 3. Sum-HEs $\mathcal{E}_{\mathrm{sum}}^{\mathrm{CB}}$ and $\mathcal{E}_{\mathrm{sum}}^{\mathrm{NCB}}$ versus the AS number K under the FPC strategy.

The behaviors of the sum-rates $\mathcal{R}_{\mathrm{sum}}^{\mathrm{CB}}$ and $\mathcal{R}_{\mathrm{sum}}^{\mathrm{NCB}}$ in Theorem 2 varying with different AS number K are depicted in Fig. 4, utilizing the same settings as in Fig. 3. Note that the simulation counterparts, which are generated by the ergodic rates in (15), are also displayed here for performance comparison. The high consistency between the simulated and analytical results corroborates the correctness of our closed-form derivations in Theorem 2. Once again, the CF architecture yields a better sum-rate than the distributed structure as previously discussed. Besides, we find all sum-rates monotonically increase with K and $\mathcal{R}_{\mathrm{sum}}^{\mathrm{NCB}}$ is significantly superior to $\mathcal{R}_{\mathrm{sum}}^{\mathrm{CB}}$ in the regimes of

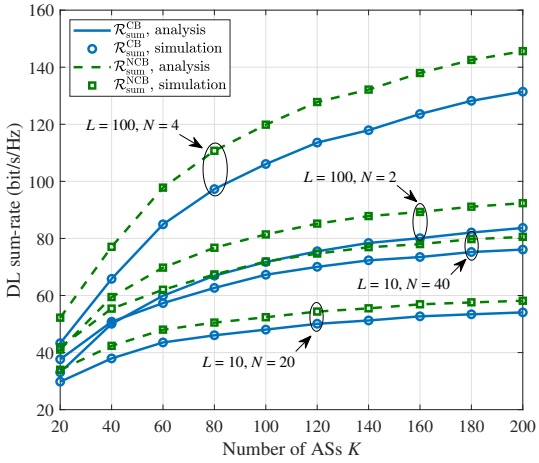

Fig. 4. Sum-rates $\mathcal{R}_{\text{sum}}^{\text{CB}}$ and $\mathcal{R}_{\text{sum}}^{\text{NCB}}$ versus the AS number K under the FPC strategy.

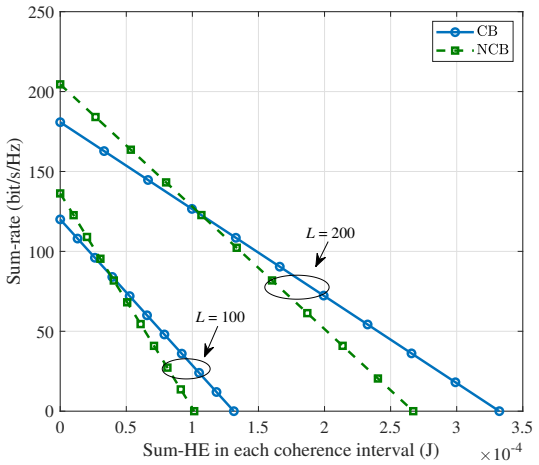

Fig. 5. Sum-rates $\mathcal{R}_{\text{sum}}^{\text{CB}}$ and $\mathcal{R}_{\text{sum}}^{\text{NCB}}$ versus sum-HEs $\mathcal{E}_{\text{sum}}^{\text{CB}}$ and $\mathcal{E}_{\text{sum}}^{\text{NCB}}$ under the FPC strategy. Here, $K = 100$ and $N = 2$.

medium and large AS number. Combined with the insights drawn from Fig. 3, it is easy to conclude that the NCB scheme is able to provide a higher sum-rate but performs unsatisfactorily in gathering RF energy as compared to the CB scheme. In the following, due to the tightness between the simulated and analytical results, we use the latter to conduct the investigation.

Fig. 5 illustrates the sum-rates $\mathcal{R}_{\text{sum}}^{\text{CB}}$ and $\mathcal{R}_{\text{sum}}^{\text{NCB}}$ as the functions of the sum-HEs $\mathcal{E}_{\text{sum}}^{\text{CB}}$ and $\mathcal{E}_{\text{sum}}^{\text{NCB}}$ against different AP number L under the FPC strategy. The HE-rate trade-off curves in Fig. 5 are generated by letting the TS factor α vary from 0 to 1, in steps of 0.1. Note that the rightmost point means the largest sum-HE while the highest point denotes the largest sum-rate. Obviously, for both CB and NCB schemes, since more time-slots are dedicated to capture energy, the sum-HEs increase with the growth of α regardless of the value of L, but this will inevitably hamper the achievable sum-rates. Besides, since increasing the AP density in a given area admits a higher degree of macro-diversity and lower path loss, the

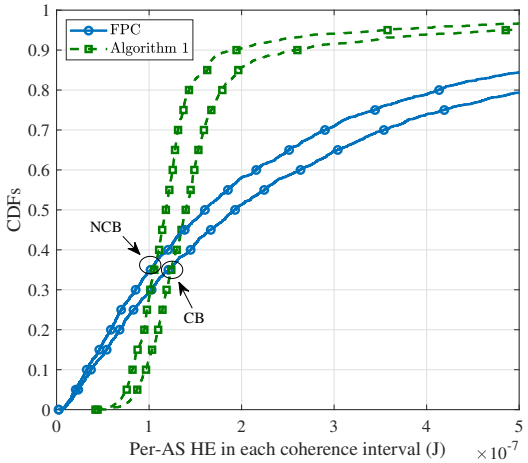

Fig. 6. CDFs of the per-AS HEs in each coherence interval $\mathcal{E}_k^{\text{CB}}$ and $\mathcal{E}_k^{\text{NCB}}$ with and without Algorithm 1. Here, $L = 60$, $K = 20$, and $N = 2$.

HE-rate trade-offs associated with "$L = 200$" greatly exceed that of "$L = 100$". Also, it should be mentioned that the slopes of the CB curves are greater than that of the NCB ones, which can be interpreted as the CB scheme can harvest more energy but achieve a lower sum-rate as compared to the NCB counterpart. This insight provides theoretical support for CF-mMIMO-based IoT SWIPT networks to choose a precoder reasonably. Aside from this, to further explore the impacts of α on the sum-HEs and sum-rates, let us denote the products of the sum-HEs and sum-rates as $\chi^{\text{CB}} \triangleq \mathcal{R}_{\text{sum}}^{\text{CB}} \times \mathcal{E}_{\text{sum}}^{\text{CB}}$ and $\chi^{\text{NCB}} \triangleq \mathcal{R}_{\text{sum}}^{\text{NCB}} \times \mathcal{E}_{\text{sum}}^{\text{NCB}}$. Considering an IoT network with $L = 200$, it has $\chi^{\text{CB}} = 10^3 \times \{0,\ 5.41,\ 9.61,\ 12.62,\ 14.42,\ 15.02,\ 14.42,\ 12.62,\ 9.61,\ 5.41,\ 0\}$ and $\chi^{\text{NCB}} = 10^3 \times \{0,\ 4.92,\ 8.74,\ 11.47,\ 13.11,\ 13.66,\ 13.11,\ 11.47,\ 8.74,\ 4.92,\ 0\}$ for α ranging from 0 to 1, in steps of 0.1. We can see that the CB scheme outperforms the NCB one in terms of χ, therefore, it is recommended to execute the CB technique at the APs to achieve a higher χ. Moreover, for both CB and NCB methods, χ is a discrete concave function with respect to α and approaches its optimum when $\alpha = 0.5$, which means that the highest χ can be arrived by halving the DL transmission time-slots.

C. APG-based Max-Min Fairness Power Control

All the above simulations are conducted on the FPC strategy. In what follows, the effectiveness of the proposed APG-based max-min fairness power control is verified. First of all, the cumulative distribution functions (CDFs) of the per-AS HEs $\mathcal{E}_k^{\text{CB}}$ and $\mathcal{E}_k^{\text{NCB}}$ with and without the proposed power optimization method are displayed in Fig. 6. Clearly, $\mathcal{E}_k^{\text{CB}}$ is higher than $\mathcal{E}_k^{\text{NCB}}$ for both FPC and Algorithm 1, which once again shows the superiority of the CB scheme in gathering RF energy. Compared with the FPC policy, the proposed max-min fairness HE algorithm can make the distributions of $\mathcal{E}_k^{\text{CB}}$ and $\mathcal{E}_k^{\text{NCB}}$ more concentrated. Quantitatively speaking, after implementing Algorithm 1, around 80% of $\mathcal{E}_k^{\text{CB}}$ and $\mathcal{E}_k^{\text{NCB}}$ fluctuate in ranges of $10^{-7} \times [0.97,\ 2.60]$ J and $10^{-7} \times [0.82,\ 1.94]$ J, respectively. The CDFs of the per-AS rates $\mathcal{R}_k^{\text{CB}}$ and $\mathcal{R}_k^{\text{NCB}}$

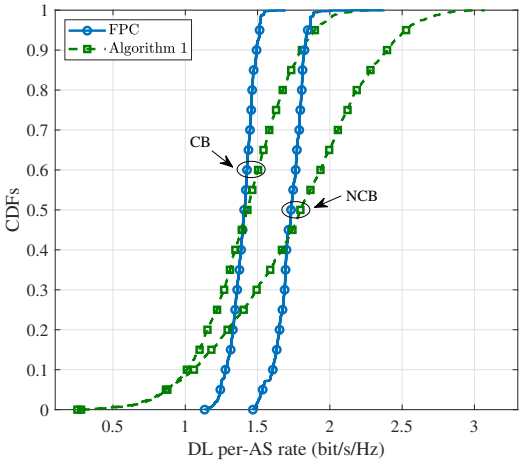

Fig. 7. CDFs of the per-AS rates $\mathcal{R}_k^{\text{NCB}}$ and $\mathcal{R}_k^{\text{NCB}}$ with and without Algorithm 1. Here, $L = 60$, $K = 20$, and $N = 2$.

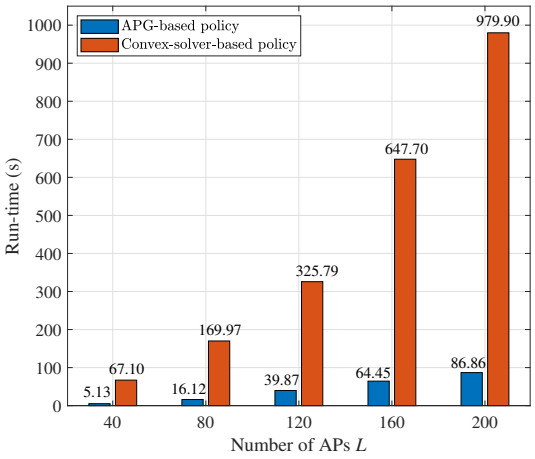

Fig. 9. Run-times of the proposed policy and the convex-solver-based policy for the CB scheme. Here, $K = 20$ and $N = 2$.

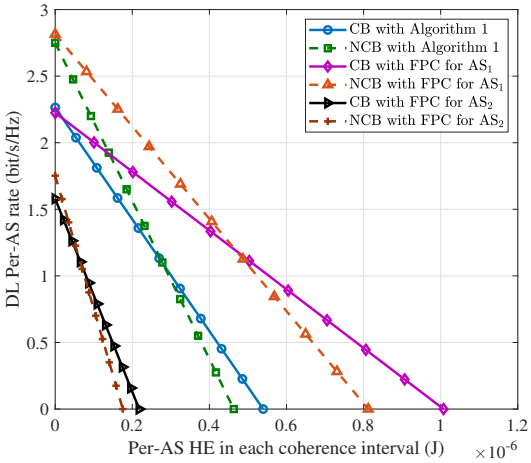

Fig. 8. Per-AS achievable rates $\mathcal{R}_k^{\text{CB}}$ and $\mathcal{R}_k^{\text{NCB}}$ versus per-AS HEs $\mathcal{E}_k^{\text{CB}}$ and $\mathcal{E}_k^{\text{NCB}}$ with and without Algorithm 1. Here, $L = 60$, $K = 20$, and $N = 2$.

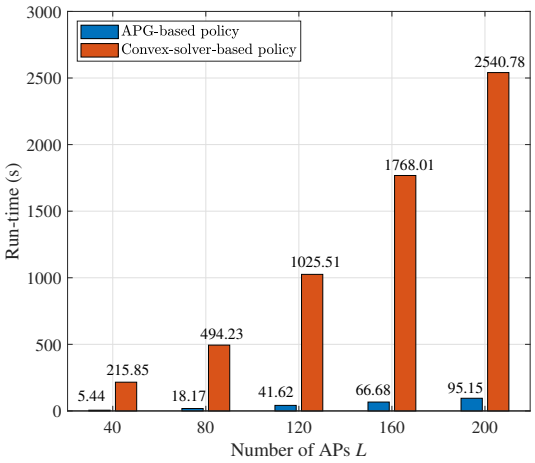

Fig. 10. Run-times of the proposed policy and the convex-solver-based policy for the NCB scheme. Here, $K = 20$ and $N = 2$.

with and without max-min fairness rate policy are depicted in Fig. 7. Same as Fig. 6, the per-AS rates associated with the proposed algorithm are much more concentrated on the median rates. For instance, about four-fifths of the rates generated by Algorithm 1 are scattered in the range of 1.27–1.49 bit/s/Hz for the CB scheme, while the range is 1.60–1.82 bit/s/Hz for the NCB case. The above observations demonstrate that the presented max-min fairness power control policy can effectively tackle the AS performance differentiation issue in CF-mMIMO-based IoT SWIPT networks.

Next, we pay attention to the DL per-AS HE-rate trade-offs under different precoding techniques and show their behaviors in Fig. 8 with both FPC and max-min fairness power control policies. Note that the max-min HE-rate trade-offs are generated by using the optimal solutions $\mathcal{E}^{\text{CB-Opt}}$, $\mathcal{R}^{\text{CB-Opt}}$, $\mathcal{E}^{\text{NCB-Opt}}$, and $\mathcal{R}^{\text{NCB-Opt}}$. Without loss of generality, Fig. 8 only concretizes the HE-rate trade-offs of AS_1 and AS_2. As can be readily observed, different ASs experience distinct HE-rate trade-offs in the context of the FPC. However, this is not the case when implementing the max-min fairness power control strategy, in which both AS_1 and AS_2 possess the same HE-rate trade-offs regardless of their geographical locations.

To conclude this section, in Figs. 9 and 10, we compare the run-times (in second) of the proposed APG-based strategy with the convex-solver-based policy for both CB and NCB schemes, respectively. Note that in Figs. 9 and 10 we focus on problems $\mathbb{R}^{\text{CB}}$ and $\mathbb{R}^{\text{NCB}}$, and the traditional convex-solver-based methods for determining the above problems are respectively presented in [21, Section IV-B] and [38, Section III-A], which are implemented by using the convex conic solver SDPT3 through the modeling tool CVX 2.1 in this work. Our simulations are developed on MATLAB 2020a and executed on a Windows 10 64-bit system with 16 GB RAM and Intel Core i7-8700, 3.2 GHz. As expected, the total run-times of the proposed strategy are far less than that of the convex-solver-based approach for both CB and NCB schemes, which confirms the merits of our proposed APG-based power control policy.

VII. Conclusions

In this work, we have conducted the performance analyses of DL CF-mMIMO-based IoT SWIPT networks in terms of the HE and achievable rate under different precoding techniques. Rigorous closed-form expressions for the underlying performance metrics with both CB and NCB schemes were respectively derived. Aside from this, we also designed an APG-based max-min fairness power control policy to provide uniform HE and achievable rate for all ASs. Extended simulation results reveals that the CB scheme harvests more wireless RF energy but yields a lower achievable rate than the NCB scheme. Besides, the proposed APG-based max-min power control strategy was more effective in guaranteeing the sensor fairness with reducing run-time.

Appendix A
Proof of Theorem 1

Since the CB scheme permits $\mathbf{w}_{lk}^{\mathrm{CB}} = \hat{\mathbf{g}}_{lk}^{*}$, $\mathcal{E}_{k}^{\mathrm{CB}}$ in (10) is computed as

$$\begin{aligned}
\mathcal{E}_{k}^{\mathrm{CB}} &= \kappa\alpha\tau_{\mathrm{d}}\rho_{\mathrm{d}}\sum_{k'=1}^{K}\mathbb{E}\left\{\left|\sum_{l=1}^{L}\sqrt{\eta_{lk'}}\mathbf{g}_{lk}^{T}\hat{\mathbf{g}}_{lk'}^{*}\right|^{2}\right\} \\
&= \kappa\alpha\tau_{\mathrm{d}}\rho_{\mathrm{d}}\sum_{k'=1}^{K}\mathbb{E}\left\{\left|\sum_{l=1}^{L}\sqrt{\eta_{lk'}}\lambda_{lk'}\mathbf{g}_{lk}^{T}\left(\mathbf{N}_{l}\boldsymbol{\varphi}_{k'}\right.\right.\right. \\
&\qquad\left.\left.\left.+\sqrt{\rho_{\mathrm{p}}\tau_{\mathrm{p}}}\sum_{k''=1}^{K}\mathbf{g}_{lk''}\boldsymbol{\varphi}_{k''}^{H}\boldsymbol{\varphi}_{k'}\right)^{*}\right|^{2}\right\} \\
&= \kappa\alpha\tau_{\mathrm{d}}\rho_{\mathrm{d}}\sum_{k'=1}^{K}\left(\mathbb{E}\left\{\left|\sum_{l=1}^{L}\sqrt{\eta_{lk'}}\lambda_{lk'}\mathbf{g}_{lk}^{T}\mathbf{N}_{l}^{*}\boldsymbol{\varphi}_{k'}^{*}\right|^{2}\right\}\right. \\
&\qquad+\rho_{\mathrm{p}}\tau_{\mathrm{p}}\mathbb{E}\left\{\left|\sum_{l=1}^{L}\sqrt{\eta_{lk'}}\lambda_{lk'}\mathbf{g}_{lk}^{T}\sum_{k''\neq k}^{K}\mathbf{g}_{lk''}^{*}\boldsymbol{\varphi}_{k''}^{T}\boldsymbol{\varphi}_{k'}^{*}\right|^{2}\right\} \\
&\qquad\left.+\rho_{\mathrm{p}}\tau_{\mathrm{p}}\mathbb{E}\left\{\left|\sum_{l=1}^{L}\sqrt{\eta_{lk'}}\lambda_{lk'}\mathbf{g}_{lk}^{T}\mathbf{g}_{lk}^{*}\boldsymbol{\varphi}_{k}^{T}\boldsymbol{\varphi}_{k'}^{*}\right|^{2}\right\}\right) \\
&\overset{(a)}{=} \kappa\alpha\tau_{\mathrm{d}}\rho_{\mathrm{d}}N\left(\sum_{k'=1}^{K}\sum_{l=1}^{L}\eta_{lk'}\beta_{lk}\gamma_{lk'}\right. \\
&\qquad\left.+N\sum_{k'=1}^{K}\left|\boldsymbol{\varphi}_{k'}^{H}\boldsymbol{\varphi}_{k}\right|^{2}\left(\sum_{l=1}^{L}\sqrt{\eta_{lk'}\gamma_{lk}\gamma_{lk'}}\right)^{2}\right), \quad (47)
\end{aligned}$$

where (a) uses [21, Eq. (54)] and $\gamma_{lk}\beta_{lk'}\beta_{lk}^{-1} = \sqrt{\gamma_{lk}\gamma_{lk'}}$ if $\boldsymbol{\varphi}_{k'} = \boldsymbol{\varphi}_{k}$. In the context of the NCB technique, we have $\mathbf{w}_{lk}^{\mathrm{NCB}} = \hat{\mathbf{g}}_{lk}^{*}/\left\|\hat{\mathbf{g}}_{lk}\right\|$. Substituting it into (10) yields

$$\mathcal{E}_{k}^{\mathrm{NCB}} = \kappa\alpha\tau_{\mathrm{d}}\rho_{\mathrm{d}}\sum_{k'=1}^{K}\mathbb{E}\left\{\left|\sum_{l=1}^{L}\sqrt{\eta_{lk'}}\mathbf{g}_{lk}^{T}\frac{\hat{\mathbf{g}}_{lk'}^{*}}{\left\|\hat{\mathbf{g}}_{lk'}\right\|}\right|^{2}\right\}. \quad (48)$$

We focus on $\mathbb{E}\left\{\left|\sum_{l=1}^{L}\sqrt{\eta_{lk'}}\mathbf{g}_{lk}^{T}\hat{\mathbf{g}}_{lk'}^{*}/\left\|\hat{\mathbf{g}}_{lk'}\right\|\right|\right\}$ and this term can be expanded into two separate terms Δ_1 and Δ_2, as

$$\begin{aligned}
&\mathbb{E}\left\{\left|\sum_{l=1}^{L}\sqrt{\eta_{lk'}}\mathbf{g}_{lk}^{T}\frac{\hat{\mathbf{g}}_{lk'}^{*}}{\left\|\hat{\mathbf{g}}_{lk'}\right\|}\right|^{2}\right\} \\
&= \sum_{l=1}^{L}\sum_{l'=1}^{L}\sqrt{\eta_{lk'}\eta_{l'k'}}\mathbb{E}\left\{\mathbf{g}_{lk}^{T}\frac{\hat{\mathbf{g}}_{lk'}^{*}\hat{\mathbf{g}}_{l'k'}^{T}}{\left\|\hat{\mathbf{g}}_{lk'}\right\|\left\|\hat{\mathbf{g}}_{l'k'}\right\|}\mathbf{g}_{l'k}^{*}\right\} \\
&= \underbrace{\sum_{l=1}^{L}\eta_{lk'}\mathbb{E}\left\{\mathbf{g}_{lk}^{T}\frac{\hat{\mathbf{g}}_{lk'}^{*}\hat{\mathbf{g}}_{lk'}^{T}}{\left\|\hat{\mathbf{g}}_{lk'}\right\|^{2}}\mathbf{g}_{lk}^{*}\right\}}_{\Delta_1} \\
&\quad+\underbrace{\sum_{l=1}^{L}\sum_{l'\neq l}^{L}\sqrt{\eta_{lk'}\eta_{l'k'}}\mathbb{E}\left\{\mathbf{g}_{lk}^{T}\frac{\hat{\mathbf{g}}_{lk'}^{*}\hat{\mathbf{g}}_{l'k'}^{T}}{\left\|\hat{\mathbf{g}}_{lk'}\right\|\left\|\hat{\mathbf{g}}_{l'k'}\right\|}\mathbf{g}_{l'k}^{*}\right\}}_{\Delta_2}. \quad (49)
\end{aligned}$$

From (49), it is straightforward to see that the calculation of Δ_1 needs to consider two separate cases with $\boldsymbol{\varphi}_{k} = \boldsymbol{\varphi}_{k'}$ and $\boldsymbol{\varphi}_{k} \neq \boldsymbol{\varphi}_{k'}$. Note that when $\boldsymbol{\varphi}_{k} = \boldsymbol{\varphi}_{k'}$, $\hat{\mathbf{g}}_{lk} = \beta_{lk}\beta_{lk'}^{-1}\hat{\mathbf{g}}_{lk'}$. By inserting this equality into Δ_1, it obtains

$$\begin{aligned}
\Delta_1 &= \sum_{l=1}^{L}\eta_{lk'}\mathbb{E}\left\{\mathbf{g}_{lk}^{T}\frac{\hat{\mathbf{g}}_{lk'}^{*}\hat{\mathbf{g}}_{lk'}^{T}}{\left\|\hat{\mathbf{g}}_{lk'}\right\|^{2}}\mathbf{g}_{lk}^{*}\right\} \\
&\overset{(b)}{=} \sum_{l=1}^{L}\eta_{lk'}\frac{\beta_{lk}^{2}}{\beta_{lk'}^{2}}\mathbb{E}\left\{\hat{\mathbf{g}}_{lk'}^{T}\frac{\hat{\mathbf{g}}_{lk'}^{*}\hat{\mathbf{g}}_{lk'}^{T}}{\left\|\hat{\mathbf{g}}_{lk'}\right\|^{2}}\hat{\mathbf{g}}_{lk'}^{*}\right\} \\
&\qquad+\sum_{l=1}^{L}\eta_{lk'}\mathbb{E}\left\{\boldsymbol{\varepsilon}_{lk}^{T}\frac{\hat{\mathbf{g}}_{lk'}^{*}\hat{\mathbf{g}}_{lk'}^{T}}{\left\|\hat{\mathbf{g}}_{lk'}\right\|^{2}}\boldsymbol{\varepsilon}_{lk}^{*}\right\} \\
&= \sum_{l=1}^{L}\eta_{lk'}\frac{\beta_{lk}^{2}}{\beta_{lk'}^{2}}\mathbb{E}\left\{\left\|\hat{\mathbf{g}}_{lk'}\right\|^{2}\right\}+\sum_{l=1}^{L}\eta_{lk'}\mathbb{E}\left\{\frac{\hat{\mathbf{g}}_{lk'}^{T}\boldsymbol{\varepsilon}_{lk}^{*}\boldsymbol{\varepsilon}_{lk}^{T}\hat{\mathbf{g}}_{lk'}^{*}}{\left\|\hat{\mathbf{g}}_{lk'}\right\|^{2}}\right\} \\
&\overset{(c)}{=} N\sum_{l=1}^{L}\eta_{lk'}\frac{\beta_{lk}^{2}}{\beta_{lk'}^{2}}\gamma_{lk'}+\sum_{l=1}^{L}\eta_{lk'}\left(\beta_{lk}-\gamma_{lk}\right) \\
&= \sum_{l=1}^{L}\eta_{lk'}\left(\left(N-1\right)\gamma_{lk}+\beta_{lk}\right), \quad (50)
\end{aligned}$$

where (b) follows from the substitution of $\mathbf{g}_{lk} = \hat{\mathbf{g}}_{lk}+\boldsymbol{\varepsilon}_{lk}$ and $\mathbb{E}\left\{\hat{\mathbf{g}}_{lk'}^{T}\boldsymbol{\varepsilon}_{lk}^{*}\right\} = 0$, and (c) is owing to (6). Besides, we stress that if $\boldsymbol{\varphi}_{k} \neq \boldsymbol{\varphi}_{k'}$, $\mathbf{g}_{lk}$ is uncorrelated with $\hat{\mathbf{g}}_{lk'}$ since $\hat{\mathbf{g}}_{lk'}$ does not contain any information with respect to $\mathbf{g}_{lk}$. Under this condition, Δ_1 is equal to

$$\begin{aligned}
\Delta_1 &= \sum_{l=1}^{L}\eta_{lk'}\mathbb{E}\left\{\frac{\hat{\mathbf{g}}_{lk'}^{T}\mathbf{g}_{lk}^{*}\mathbf{g}_{lk}^{T}\hat{\mathbf{g}}_{lk'}^{*}}{\left\|\hat{\mathbf{g}}_{lk'}\right\|^{2}}\right\} \\
&= \sum_{l=1}^{L}\eta_{lk'}\mathbb{E}\left\{\frac{\hat{\mathbf{g}}_{lk'}^{T}\mathbb{E}\left\{\mathbf{g}_{lk}^{*}\mathbf{g}_{lk}^{T}\right\}\hat{\mathbf{g}}_{lk'}^{*}}{\left\|\hat{\mathbf{g}}_{lk'}\right\|^{2}}\right\} \\
&= \sum_{l=1}^{L}\eta_{lk'}\beta_{lk}. \quad (51)
\end{aligned}$$

Until now, the quantity Δ_2 in (49) has not yet been computed. From Δ_2, it is straightforward to conclude that only when $\boldsymbol{\varphi}_{k} = \boldsymbol{\varphi}_{k'}$, the value of Δ_2 is not zero. By inserting $\hat{\mathbf{g}}_{lk} = \beta_{lk}\beta_{lk'}^{-1}\hat{\mathbf{g}}_{lk'}$ into Δ_2, Δ_2 is further written as

$$\begin{aligned}
\Delta_2 &= \sum_{l=1}^{L}\sum_{l'\neq l}^{L}\sqrt{\eta_{lk'}\eta_{l'k'}}\mathbb{E}\left\{\mathbf{g}_{lk}^{T}\frac{\hat{\mathbf{g}}_{lk'}^{*}\hat{\mathbf{g}}_{l'k'}^{T}}{\left\|\hat{\mathbf{g}}_{lk'}\right\|\left\|\hat{\mathbf{g}}_{l'k'}\right\|}\mathbf{g}_{l'k}^{*}\right\} \\
&= \sum_{l=1}^{L}\sum_{l'\neq l}^{L}\sqrt{\eta_{lk'}\eta_{l'k'}}\frac{\beta_{lk}\beta_{l'k}}{\beta_{lk'}\beta_{l'k'}}\mathbb{E}\left\{\left\|\hat{\mathbf{g}}_{lk'}\right\|\right\}\mathbb{E}\left\{\left\|\hat{\mathbf{g}}_{l'k'}\right\|\right\}
\end{aligned}$$

$$\overset{(d)}{=} \Gamma_N^2 \sum_{l=1}^{L} \sum_{l' \neq l}^{L} \sqrt{\eta_{lk'} \eta_{l'k'}} \frac{\beta_{lk} \beta_{l'k}}{\beta_{lk'} \beta_{l'k'}} \sqrt{\gamma_{lk'} \gamma_{l'k'}}$$
$$\overset{(e)}{=} \Gamma_N^2 \sum_{l=1}^{L} \sum_{l' \neq l}^{L} \sqrt{\eta_{lk'} \eta_{l'k'}} \sqrt{\gamma_{lk} \gamma_{l'k}}, \tag{52}$$

where in (d) we use $\mathbb{E}\{\|\hat{\mathbf{g}}_{lk'}\|\} = \Gamma_N \sqrt{\gamma_{lk'}}$ with $\Gamma_N = \Gamma(N+1/2)/\Gamma(N)$ and (e) is obtained by using $\beta_{lk'} \beta_{lk}^{-1} = \sqrt{\gamma_{lk'} \gamma_{lk}^{-1}}$. Plugging (50)–(52) into (49) and substituting the obtained (49) into (48), $\mathcal{E}_k^{\text{NCB}}$ is proved.

Appendix B
Proof of Theorem 2

We begin with the proof of $\mathcal{R}_k^{\text{CB}}$. Bearing in mind that $\mathbf{w}_{lk}^{\text{CB}} = \hat{\mathbf{g}}_{lk}^*$ and the channel estimate and estimate error are uncorrelated under the MMSE property, $\mathbb{E}\left\{\mathbf{g}_{lk}^T \hat{\mathbf{g}}_{lk}^*\right\}$ equals

$$\mathbb{E}\left\{\mathbf{g}_{lk}^T \hat{\mathbf{g}}_{lk}^*\right\} = \mathbb{E}\left\{\left(\hat{\mathbf{g}}_{lk}^T + \boldsymbol{\varepsilon}_{lk}^T\right) \hat{\mathbf{g}}_{lk}^*\right\} = N \gamma_{lk}. \tag{53}$$

Next, the variance of $\sum_{l=1}^{L} \sqrt{\eta_{lk}} \mathbf{g}_{lk}^T \mathbf{w}_{lk}$ is computed as

$$\begin{aligned}
&\text{Var}\left(\sum_{l=1}^{L} \sqrt{\eta_{lk}} \mathbf{g}_{lk}^T \hat{\mathbf{g}}_{lk}^*\right) \\
&= \mathbb{E}\left\{\left|\sum_{l=1}^{L} \sqrt{\eta_{lk}} \mathbf{g}_{lk}^T \hat{\mathbf{g}}_{lk}^*\right|^2\right\} - \left|\mathbb{E}\left\{\sum_{l=1}^{L} \sqrt{\eta_{lk}} \mathbf{g}_{lk}^T \hat{\mathbf{g}}_{lk}^*\right\}\right|^2 \\
&\overset{(f)}{=} N \sum_{l=1}^{L} \eta_{lk} \beta_{lk} \gamma_{lk} + N^2 \left(\sum_{l=1}^{L} \sqrt{\eta_{lk}} \gamma_{lk}\right)^2 \\
&\qquad - N^2 \left(\sum_{l=1}^{L} \sqrt{\eta_{lk}} \gamma_{lk}\right)^2 \\
&= N \sum_{l=1}^{L} \eta_{lk} \beta_{lk} \gamma_{lk},
\end{aligned} \tag{54}$$

where (f) is obtained by letting $k' = k$ in (47). By subtracting the terms associated with $k' = k$ in (47), the third expectation in (15) when considering the CB scheme is written as

$$\begin{aligned}
&\rho_{\text{d}} \sum_{k' \neq k}^{K} \mathbb{E}\left\{\left|\sum_{l=1}^{L} \sqrt{\eta_{lk'}} \mathbf{g}_{lk}^T \hat{\mathbf{g}}_{lk'}^*\right|^2\right\} \\
&= N \left(N \sum_{k'=1}^{K} \left|\boldsymbol{\varphi}_{k'}^H \boldsymbol{\varphi}_k\right|^2 \left(\sum_{l=1}^{L} \sqrt{\eta_{lk'} \gamma_{lk} \gamma_{lk'}}\right)^2 \right. \\
&\qquad \left. + \sum_{k'=1}^{K} \sum_{l=1}^{L} \eta_{lk'} \beta_{lk} \gamma_{lk'}\right).
\end{aligned} \tag{55}$$

Plugging (53)–(55) into (15) and performing some linear algebraic operations, (16) is proved. We stress that the proof of (17) can be finished by following the same techniques in deriving (12) and (16), the detailed procedures are omitted here.

References

[1] J. Huang, Y. Meng, X. Gong, Y. Liu, and Q. Duan, "A novel deployment scheme for green Internet of things," *IEEE Internet Things J.*, vol. 1, no. 2, pp. 196–205, Apr. 2014.

[2] L. D. Xu, W. He, and S. Li, "Internet of things in industries: A survey," *IEEE Trans. Ind. Inf.*, vol. 10, no. 4, pp. 2233–2243, Nov. 2014.

[3] A. Al-Fuqaha, M. Guizani, M. Mohammadi, M. Aledhari, and M. Ayyash, "Internet of things: A survey on enabling technologies, protocols, and applications," *IEEE Commun. Surveys Tuts.*, vol. 17, no. 4, pp. 2347–2376, 4th Quart., 2015.

[4] F. Javed, M. K. Afzal, M. Sharif, and B. Kim, "Internet of things (IoT) operating systems support, networking technologies, applications, and challenges: A comparative review," *IEEE Commun. Surveys Tuts.*, vol. 20, no. 3, pp. 2062–2100, 3rd Quart., 2018.

[5] Z. Chu, F. Zhou, Z. Zhu, R. Q. Hu, and P. Xiao, "Wireless powered sensor networks for Internet of things: Maximum throughput and optimal power allocation," *IEEE Internet Things J.*, vol. 5, no. 1, pp. 310–321, Feb. 2018.

[6] R. Zhang and C. K. Ho, "MIMO broadcasting for simultaneous wireless information and power transfer," *IEEE Trans. Wireless Commun.*, vol. 12, no. 5, pp. 1989–2001, May 2013.

[7] L. Liu, R. Zhang, and K. Chua, "Wireless information and power transfer: A dynamic power splitting approach," *IEEE Trans. Commun.*, vol. 61, no. 9, pp. 3990–4001, Sept. 2013.

[8] X. Wang and C. Zhai, "Simultaneous wireless information and power transfer for downlink multi-user massive antenna-array systems," *IEEE Trans. Commun.*, vol. 65, no. 9, pp. 4039–4048, Sept. 2017.

[9] Z. Ding, C. Zhong, D. W. K. Ng, M. Peng, H. A. Suraweera, R. Schober, and H. V. Poor, "Application of smart antenna technologies in simultaneous wireless information and power transfer," *IEEE Commun. Mag.*, vol. 53, no. 4, pp. 86–93, Apr. 2015.

[10] J. Zhu, Y. Li, N. Wang, and W. Xu, "Wireless information and power transfer in secure massive MIMO downlink with phase noise," *IEEE Wireless Commun. Lett.*, vol. 6, no. 3, pp. 298–301, Jun. 2017.

[11] P. Liu, Q. Zhang, J. Wang, D. Kong, and Y. Zhang, "Statistical description of channel estimation error in massive MIMO systems with Ricean fading," *IEEE Trans. Veh. Technol.*, 2021, to appear.

[12] J. Xu, W. Xu, H. Zhang, G. Y. Li, and X. You, "Performance analysis of multi-cell millimeter wave massive MIMO network with low-precision ADCs," *IEEE Trans. Commun.*, vol. 67, no. 1, pp. 302–317, Jan. 2019.

[13] M. He, W. Xu, H. Shen, C. Pan, C. Zhao, and G. Xie, "Is multipath channel beneficial for wideband massive MIMO with low-resolution ADCs?" *IEEE Trans. Commun.*, vol. 69, no. 9, pp. 4083–4097, Jun. 2021

[14] G. Dong, H. Zhang, and D. Yuan, "Downlink achievable rate of massive MIMO enabled SWIPT systems over Rician channels," *IEEE Commun. Lett.*, vol. 22, no. 3, pp. 578–581, Mar. 2018.

[15] A. Thakur and R. C. Mishra, "Performance analysis of energy-efficient multi-cell massive MIMO system," in *Proc. Int. Conf. Comput. Commun. Networking Technol. (ICCCNT)*, Kanpur, India, 2019, pp. 1–7.

[16] Z. Goli, S. M. Razavizadeh, H. Farhadi, and T. Svensson, "Secure simultaneous information and power transfer for downlink multi-user massive MIMO," *IEEE Access*, vol. 8, pp. 150514–150526, 2020.

[17] X. Wang, A. Ashikhmin, and X. Wang, "Wirelessly powered cell-free IoT: Analysis and optimization," *IEEE Internet Things J.*, vol. 7, no. 9, pp. 8384–8396, Sept. 2020.

[18] X. Wang, X. Wang, and A. Ashikhmin, "Long-term scheduling and power control for wirelessly powered cell-free IoT," *IEEE Internet Things J.*, vol. 8, no. 1, pp. 332–344, Jan., 2021.

[19] W. Xia, G. Zheng, Y. Zhu, J. Zhang, J. Wang, and A. P. Petropulu, "A deep learning framework for optimization of MISO downlink beamforming," *IEEE Trans. Commun.*, vol. 68, no. 3, pp. 1866–1880, Mar. 2020.

[20] W. Xia, T. Q. S. Quek, K. Guo, W. Wen, H. H. Yang and H. Zhu, "Multi-armed bandit based client scheduling for federated learning," *IEEE Trans. Wireless Commun.*, vol. 19, no. 11, pp. 7108–7123, Nov. 2020.

[21] H. Q. Ngo, A. Ashikhmin, H. Yang, E. G. Larsson, and T. L. Marzetta, "Cell-free massive MIMO versus small cells," *IEEE Trans. Wireless Commun.*, vol. 16, no. 3, pp. 1834–1850, Mar. 2017.

[22] H. Q. Ngo, L. Tran, T. Q. Duong, M. Matthaiou, and E. G. Larsson, "On the total energy efficiency of cell-free massive MIMO," *IEEE Trans. Green Commun. Netw.*, vol. 2, no. 1, pp. 25–39, Mar. 2018.

[23] Y. Zhang, M. Zhou, H. Cao, L. Yang, and H. Zhu, "On the performance of cell-free massive MIMO with mixed-ADC under Rician fading channels," *IEEE Commun. Lett.*, vol. 24, no. 1, pp. 43–47, Jan. 2020.

[24] H. Yang and T. L. Marzetta, "Energy efficiency of massive MIMO: Cell-free vs. cellular," in *Proc. IEEE Veh. Technol. Conf. (VTC)*, Porto, Portugal, 2018, pp. 1–5.

[25] D. Kudathanthirige, R. Shrestha, and G. A. A. Baduge, "Max-min fairness optimal rate-energy trade-off of SWIPT for massive MIMO downlink," *IEEE Commun. Lett.*, vol. 23, no. 4, pp. 688–691, Apr. 2019.

[26] D. L. Galappaththige, R. Shrestha, and G. A. A. Baduge, "Exploiting cell-free massive MIMO for enabling simultaneous wireless information and power transfer," *IEEE Trans. Green Commun. Netw.*, early access, doi: 10.1109/TGCN.2021.3090357.

[27] M. Bashar, K. Cumanan, A. G. Burr, M. Debbah, and H. Q. Ngo, "Enhanced max-min SINR for uplink cell-free massive MIMO systems," in *Proc. IEEE Int. Conf. Commun. (ICC)*, Kansas City, MO, 2018, pp. 1–6.

[28] M. Bashar, K. Cumanan, A. G. Burr, H. Q. Ngo, and H. V. Poor, "Mixed quality of service in cell-free massive MIMO," *IEEE Commun. Lett.*, vol. 22, no. 7, pp. 1494–1497, Jul. 2018.

[29] G. Interdonato, H. Q. Ngo, E. G. Larsson, and P. Frenger, "On the performance of cell-free massive MIMO with short-term power constraints," in *Proc. IEEE Int. Workshop Comput. Aided Modell. Des. Commun. Links Networks (CAMAD)*, Toronto, ON, 2016, pp. 225–230.

[30] H. Li and Z. Lin, "Accelerated proximal gradient methods for nonconvex programming," *Adv. Neural Inf. Process. Syst. 28*, C. Cortes, N. D. Lawrence, D. D. Lee, M. Sugiyama, and R. Garnett, Eds. Curran Associates, Inc., 2015, pp. 379–387.

[31] M. Farooq, H. Q. Ngo, and L. N. Tran, "Accelerated projected gradient method for the optimization of cell-free massive MIMO downlink," in *Proc. IEEE Annu. Int. Symp. Pers. Indoor Mob. Radio Commun.*, London, United Kingdom, 2020, pp. 1–6.

[32] L. Tran and H. Q. Ngo, "First-order methods for energy-efficient power control in cell-free massive MIMO: Invited paper," in *Proc. Asilomar Conf. Signals, Syst. Comput. (ACSSC)*, Pacific Grove, CA, USA, 2019, pp. 848–852.

[33] G. Dong, X. Zhou, H. Zhang, and D. Yuan, "Achievable rate optimization for massive MIMO enabled SWIPT systems over downlink Rician channels," *IEEE Access*, vol. 6, pp. 36810–36824, 2018.

[34] G. Yang, C. K. Ho, R. Zhang, and Y. L. Guan, "Throughput optimization for massive MIMO systems powered by wireless energy transfer," *IEEE J. Sel. Areas Commun.*, vol. 33, no. 8, pp. 1640–1650, Aug. 2015.

[35] Y. Zhu, L. Wang, K.-K. Wong, S. Jin, and Z. Zheng, "Wireless power transfer in massive MIMO-aided HetNets with user association," *IEEE Trans. Commun.*, vol. 64, no. 10, pp. 4181–4195, Oct. 2016.

[36] Y. Nesterov, "Smooth minimization of non-smooth functions," *Math. Program.*, Ser. A, vol. 103, pp. 127–152, 2005.

[37] H. H. Bauschke, M. N. Bui, and X. Wang, "Projecting onto the intersection of a cone and a sphere," *SIAM J. Optim.*, vol. 28, no. 3, pp. 2158–2188, Jan. 2018.

[38] Y. Zhang, H. Cao, C. Qi, P. Zhong, and L. Yang, "Power optimization in cell-free massive MIMO with short-term power constraints," in *Proc. IEEE Int. Conf. Comput. Commun. (ICCC)*, Chengdu, China, 2018, pp. 370–376.